Mechanism and Machine Theory 168 (2022) 104608

Contents lists available at ScienceDirect

Mechanism and Machine Theory

journal homepage: www.elsevier.com/locate/mechmt

Wind deflection analysis of railway catenary under crosswind based on nonlinear finite element model and wind tunnel test

Yang Song [a], Mingjie Zhang [b,*], Ole Øiseth [c], Anders Rønnquist [d]

[a] Department of Structural Engineering, Norwegian University of Science and Technology, Trondheim 7491, Norway
[b] Department of Structural Engineering, Norwegian University of Science and Technology, Trondheim 7491, Norway
[c] Department of Structural Engineering, Norwegian University of Science and Technology, Trondheim 7491, Norway
[d] Department of Structural Engineering, Norwegian University of Science and Technology, Trondheim 7491, Norway

ARTICLE INFO

Keywords:
Electrified railway
Catenary
Finite element
Wind deflection
Contact wire
Crosswind

ABSTRACT

This paper evaluates the railway catenary's wind deflection under crosswind based on wind tunnel experiments and a nonlinear finite element model. A catenary model is constructed based on the absolute nodal coordinate formulation to describe the geometrical nonlinearity of the system. The aerodynamic forces acting on the catenary are derived according to the quasi-steady theory, and the aerodynamic coefficients are obtained by wind tunnel experiments. A procedure to generate the three-dimensional fluctuating wind field along the catenary is presented. The extreme value of the wind deflection is estimated based on a Poisson approximation of the extreme value distribution. The numerical accuracy is validated by wind tunnel experimental results of an aeroelastic catenary. The response, statistics, frequency characteristics and extreme value of the contact wire's wind deflection are investigated through numerical simulations. The analysis results indicate that the maximum wind deflection will exceed the safety limit for the analysed catenary with a turbulence intensity of more than 15%. The adjustment of some critical parameters of the catenary system can reduce the maximum wind deflection.

1. Introduction

The railway catenary is constructed along the track to power the electric train, as shown in Fig. 1. The electric current transmits from the contact wire to the engine through the pantograph mounted on the train roof. A safe and stable sliding contact between the pantograph and catenary is of great importance for enabling fast trains without traffic interruptions [1]. The catenary is a long-span and high-flexibility structure that is susceptible to wind loads. The wind load may cause a large deflection of the contact wire and affect reliable contact with pantograph collectors.

1.1. Problem description

There are several forms of wind-induced vibration for long-span structures [2], including buffeting [3], galloping [4], vortex-excited vibration [5] and flutter [6]. Amongst these, buffeting and galloping are two primary wind-induced vibrations for the catenary. The former is a forced vibration caused by stochastic winds [3], while the latter is an aerodynamic instability induced by

* Corresponding author.
E-mail address: mingjie.zhang@ntnu.no (M. Zhang).

https://doi.org/10.1016/j.mechmachtheory.2021.104608
Received 21 July 2021; Received in revised form 19 October 2021; Accepted 19 October 2021
Available online 28 October 2021

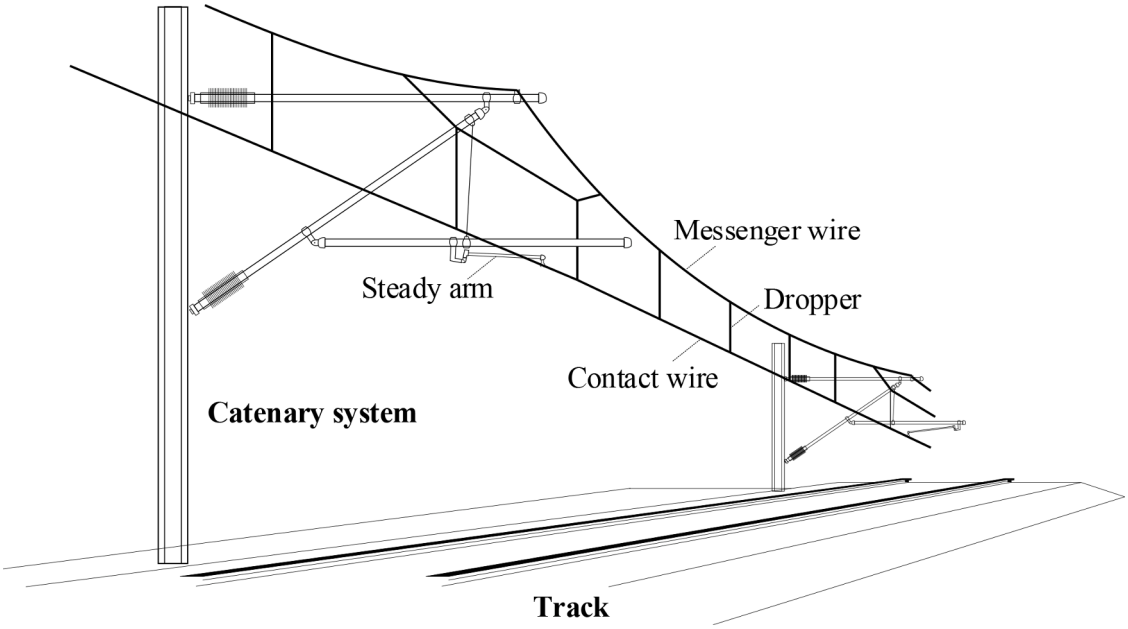

Fig. 1. Schematics of catenary system.

self-excited forces [7]. Although galloping may cause a large amplitude and destructive damage to the catenary [8], this only occurs in extreme conditions and is rarely observed. By contrast, the buffeting of the catenary is a common phenomenon that often occurs in daily operations and threatens the safety and reliability of the railway system. More specifically, the contact wire may deviate in the lateral direction due to crosswinds, which further results in the dewirement and scraping of the pantograph collector. Dewirement may bring about fatal accidents such as pantograph collapse and contact wire breakage, which cause traffic disorders and even threaten passengers' lives. Thus, to avoid these accidents, the maximum wind deflection of the contact wire must be strictly limited within the safe working range of the pantograph collector.

1.2. Review of current research

The operating safety of railways is an important priority for all rail operators around the world and is of ever-increasing importance for the improvement and maintenance of vehicles [9,10] and infrastructures [11]. The catenary has been widely recognised as the most vulnerable part of a traction power system [12,13]. The interaction between the pantograph and catenary is one of three critical coupling relationships in modern electrified railways: wheel-rail [14], fluid-structure [15] and pantograph-catenary [16]. Many scholars have devoted their attention to a mathematical description of the catenary's dynamic behaviour subject to the impact of pantograph and environmental loads [17,18]. The dynamic response of the catenary subject to moving pantographs was evaluated by means of the finite element method (FEM) [19], analytical solution [20] and experimental test [21]. Typical disturbances such as defective droppers [22], irregularities [23,24] and wave propagation [25] were adequately described in the catenary model.

The catenary exhibits large deformation when it is subjected to a wind load. To describe the catenary's geometrical nonlinearity, a flexible cable element [26] and absolute nodal coordinate formulation (ANCF) [27,28] have been widely employed to model the catenary. A 2D wind field was constructed along the catenary by Pombo et al. [29,30] and Song et al. [31] to investigate the wind-induced vibration's effect on the contact force. Then, a similar work was performed with a 3D wind field [32]. A catenary aeroelastic model was first built by Xie et al. [33] to evaluate the wind-induced response with different tension classes.

The catenary's wind deflection has also attracted much attention from the industry. The current technical specification [34,35] specifies that the wind deflection of the contact wire must be restricted within the operating range of the pantograph collector. The wind load acting on the contact wire can be calculated by

$$q_{\mathrm{K}} = \frac{1}{2} G_{\mathrm{q}} G_{\mathrm{t}} \rho V_{\mathrm{R}}^2 \tag{1}$$

in which G_{q} is the gust response factor. G_{t} is the terrain factor taking into account the protection of wires, e.g. in cuts, cities or forests. V_{R} is the reference wind velocity at a height of 10 m above ground. Most coefficients in this formula are defined by experience. The drag and lift coefficients of a realistic contact wire cross-section essential to determine the aerodynamics are not included in the formula. Eq. (1) does not fully account for the contribution of the fluctuating wind. Then, q_{K} is substituted in the following empirical equation [34] to estimate the maximum wind deviation $e_{\max}$ of the contact wire.

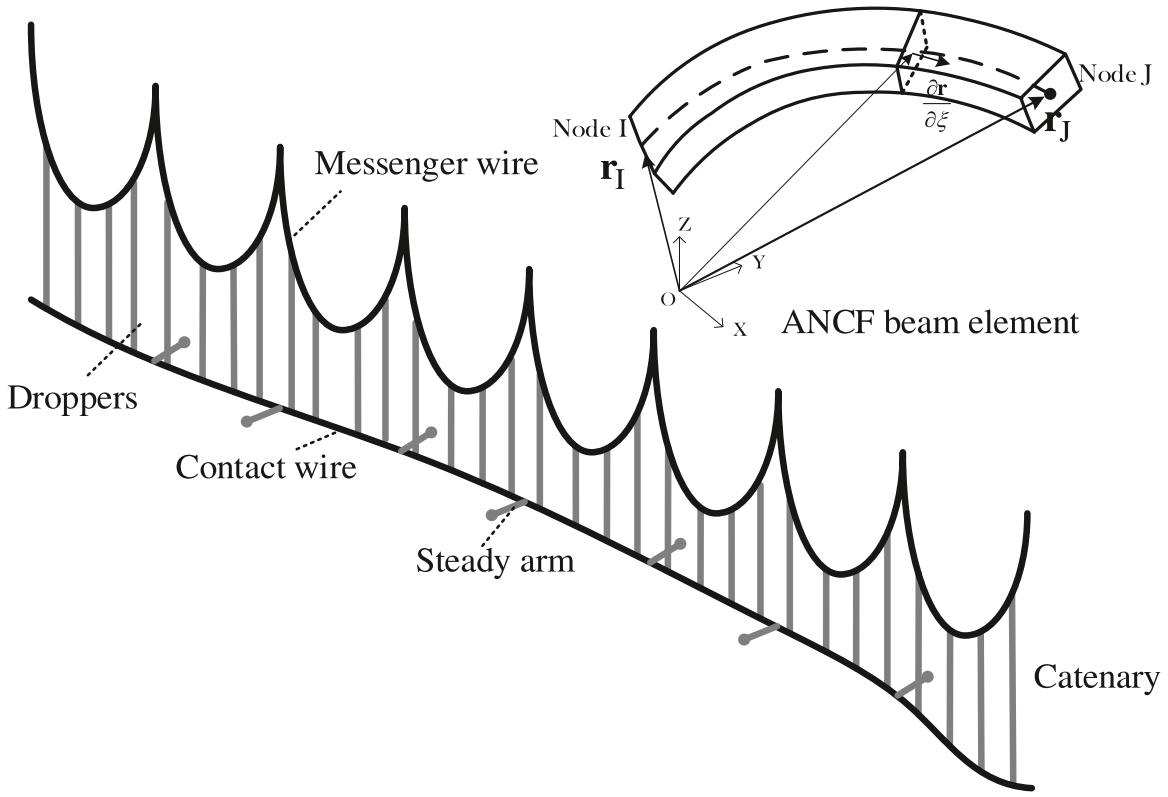

Fig. 2. Catenary model and ANCF beam element.

$$e_{\max} = \frac{q_K L_p^2}{8T} + \frac{2T{L_{st}}^2}{q_K L_p^2} \tag{2}$$

in which L_{st} is the stagger value, T is the contact wire tension and L_p is the span length. The empirical equation is derived based on the uniformly distributed load acting on the tensioned cable. However, the catenary has a much more complex structure and strong nonlinearity. A nonlinear finite element approach is desired to reproduce more realistic behaviours of a catenary with fluctuating wind.

1.3. Contributions of this paper

Through the above literature review, some shortcomings in the current research are summarised as follows:

1) In [29,30], the contact-wire cross section is assumed to be a perfectly circular section that cannot accurately describe the aerodynamic property of an actual contact wire. Even though a realistic cross-sectional profile was considered in [8,31] to measure the contact wire's aerodynamic coefficients, the numerically obtained aerodynamic coefficients required further validation before they can be used to calculate the wind loads.
2) Most previous works [30,32] focused on the vertical vibration caused by the wind load, which directly affects the contact force. However, fatal accidents such as the dewirement and scarping of the pantograph collector are caused mainly by the lateral wind deflection of the contact wire.
3) In current industry, the maximum wind deflection of the contact wire is estimated by an empirical equation [34], which should be compared with FEM results. In particular, the fluctuating wind may cause a sizeable transient deviation of the contact wire, which may exceed the working range of the pantograph head.

The above issues are addressed in this paper. A nonlinear finite element model of the catenary is built to study the contact wire's wind deflection. The aerodynamic forces acting on the catenary are derived from quasi-steady aerodynamic theory. Wind tunnel experiments are conducted to obtain the aerodynamic coefficients of the contact wire. A 3D fluctuating wind field along the catenary is constructed, and the equation of motion for the catenary is solved iteratively to obtain the catenary's wind-induced response. According to the simulation results, the extreme value of the wind deflection is estimated based on Davenport's empirical distribution. The effect of the turbulence intensity on the contact wire wind deflection is evaluated through a series of numerical simulations. The

sensitivity of the catenary's key parameters to the wind deflection is also investigated.

2. Finite element model of catenary

The catenary is comprised of five main components: contact wire, messenger wire, dropper and steady arm. These are illustrated in Fig. 2. The contact wire is responsible for transmitting the electric current to the pantograph. The messenger wire and droppers are used to support the contact wire, keeping it at the design height. To adequately describe the catenary's nonlinearity in wind-induced vibration, an absolute nodal coordinate formulation (ANCF) beam element is utilised to model the contact wire and messenger wire. The slackness of the dropper is modelled by a cable element with nonlinear axial stiffness. The steady arm is assumed to be a truss element that can rotate around the support point in the contact wire. The claws on clamps are simplified as lumped masses in the messenger/contact wires. The initial configuration of the catenary is calculated using the target configuration under dead loads (TCUD) method. The present model was validated to have good accuracy in evaluating the dynamic response of pantograph-catenary interactions [21].

2.1. ANCF beam element

In this work, an ANCF beam with 12 degrees of freedom (DOFs) is adopted to discretise the contact and messenger wires. The DOF vector for each element can be written as follows:

$$\mathbf{e} = \left[x_i \quad y_i \quad z_i \quad \frac{\partial x_i}{\partial \chi} \quad \frac{\partial y_i}{\partial \chi} \quad \frac{\partial z_i}{\partial \chi} \quad x_j \quad y_j \quad z_j \quad \frac{\partial x_j}{\partial \chi} \quad \frac{\partial y_j}{\partial \chi} \quad \frac{\partial z_j}{\partial \chi} \right]^{\mathrm{T}} \tag{3}$$

in which χ is the local coordinate from 0 to element length L_0. The generalised elastic force vector $\mathbf{Q_e}$ can be seen as the summation of the contribution from the bending and axial strain deformations.

$$\mathbf{Q_e} = \frac{1}{2}\int_0^{L_0} \left(EA \frac{\partial}{\partial \mathbf{e}} \varepsilon_l^2 + EI \frac{\partial}{\partial \mathbf{e}} \kappa^2 \right) d\chi \tag{4}$$

in which E is Young's modulus, A is the cross-sectional area, I is the moment inertia of the wire. The solution of Eq. (4) normally has complex mathematical expressions. A necessary simplification is desired to be performed based on the continuum mechanics assumption. The global position vector $\mathbf{r}$ of an arbitrary point can be calculated by the product of $\mathbf{e}$ and the shape function matrix $\mathbf{S}$ as

$$r = Se \tag{5}$$

where $\mathbf{S}$ can be defined as follows:

$$\begin{aligned} \mathbf{S} &= \begin{bmatrix} S_1 & & & S_2 & & & S_3 & & & S_4 & & \\ & S_1 & & & S_2 & & & S_3 & & & S_4 & \\ & & S_1 & & & S_2 & & & S_3 & & & S_4 \end{bmatrix} \\ S_1(\xi) &= 1 - 3\xi^2 + 2\xi^3 \\ S_2(\xi) &= L_0\left(\xi + \xi^3 - 2\xi^2\right) \\ S_3(\xi) &= 3\xi^2 - 2\xi^3 \\ S_4(\xi) &= L_0\left(\xi^3 - \xi^2\right) \end{aligned} \tag{6}$$

in which ξ is the normalised coordinate, which can be calculated by $\xi = \chi/L_0$. The longitudinal strain ε_l and the curvature κ can be expressed by

$$\begin{aligned} \varepsilon_l &= \frac{1}{2}\left(\mathbf{r}_\chi \mathbf{r}_\chi - 1\right) \\ \kappa &= \frac{\left|\mathbf{r}_\chi \times \mathbf{r}_{\chi\chi}\right|}{\left|\mathbf{r}_\chi\right|^3} \end{aligned} \tag{7}$$

in which

$$\begin{aligned} \mathbf{r}_\chi &= \frac{\mathrm{d}\mathbf{S}}{\mathrm{d}\xi}\mathbf{e} \Big/ L_0 \\ \mathbf{r}_{\chi\chi} &= \frac{\mathrm{d}^2\mathbf{S}}{\mathrm{d}\xi^2}\mathbf{e} \Big/ L_0^2 \end{aligned} \tag{8}$$

Substituting Eq. (7) into Eq. (4) yields the secant stiffness matrix $\mathbf{K}_e$ as follows:

$$\mathbf{Q}_e = \mathbf{K}_e \mathbf{e} \tag{9}$$

The tangent stiffness matrices are primarily used in the shape-finding procedure. In the dynamic simulation, the tangent stiffness

Table 1
Parameters of catenary.

Span length	60 m
Contact Wire Tension	13 kN
Messenger Wire Tension	13 kN
Contact Wire Area	120 mm^2
Messenger Wire Area	120 mm^2
Contact Wire Linear Density	1.07 kg/m
Messenger Wire Linear Density	1.06 kg/m

matrix is most commonly used in an explicit integration algorithm. Thus, the corresponding tangent stiffness matrices $\mathbf{K}_T$ and $\mathbf{K}_L$ can be derived by taking part of Eq. (9) against $\mathbf{e}$ and L_0 as follows:

$$\Delta\mathbf{F} = \frac{\partial\mathbf{Q}}{\partial\mathbf{e}}\Delta\mathbf{e} + \frac{\partial\mathbf{Q}}{\partial L_0}\Delta L_0 = \mathbf{K}_T\Delta\mathbf{e} + \mathbf{K}_L\Delta L_0 \tag{10}$$

A similar derivation can be used to obtain the tangent stiffness matrices of the cable element (used for droppers) and the truss element (used for the steady arm). Note that the axial stiffness changes to zero when the dropper works in compression.

2.2. Catenary model

Using a classic FEM approach, the stiffness matrix of each element can be assembled to generate the global incremental equilibrium equation for the entire catenary as follows:

$$\Delta\mathbf{F}^G = \mathbf{K}_T^G\Delta\mathbf{U}_C + \mathbf{K}_L^G\Delta\mathbf{L}_0 \tag{11}$$

where $\Delta\mathbf{F}^G$ is the global unbalanced force vector. $\mathbf{K}_T^G$ and $\mathbf{K}_L^G$ are the global stiffness matrices related to the incremental nodal displacement vector $\Delta\mathbf{U}_C$ and the incremental unstrained length vector $\Delta\mathbf{L}_0$, respectively. The initial configuration of the catenary can be calculated by solving Eq. (11). However, Eq. (11) cannot be solved directly, as the number of equations is smaller than the number of unknowns. The idea of TCUD is to introduce additional constraints equal to the total number of beam or cable elements [36]. According to [28], three types of additional constraint conditions are used here. These are usually determined by the design specifications and the measurement geometry data. Thus, $\begin{bmatrix}\mathbf{K}_T^G & \mathbf{K}_L^G\end{bmatrix}$ in Eq. (11) can be reduced to a square matrix, which ensures equality between the number of equations and the number of unknowns. The steady arm points are fixed tentatively in the shape-finding procedure to ensure that the support points are at their correct positions. Afterward, the inclination of each steady arm is calculated by the resistance forces in the fixed point. Then, the steady arm point constraints are removed and replaced by a rigid truss element with the proper inclination to reproduce the realistic behaviour of a steady arm.

Table 1 presents the main parameters of a catenary used in a typical conventional-speed railway. The initial configuration of the catenary can be calculated according to the previous procedure. As the catenary is a periodical structure, the behaviours of wind-induced vibration are almost the same for each span (especially the lateral wind deflection). Catenaries with a few spans can be used to study the wind-induced response to save computational effort. The central two spans are taken as the analysis object in the subsequent sections to avoid the boundary effect.

After obtaining the initial configuration, the global stiffness matrix $\mathbf{K}_T^G$ can be obtained in the equilibrium state. In combination with a consistent mass matrix $\mathbf{M}_T^G$ and damping matrix $\mathbf{C}_T^G$, the equation of motion for the catenary subjected to an external force vector $\mathbf{F}_T^G(t)$ can be written as

$$\mathbf{M}_T^G\ddot{\mathbf{U}}_C(t) + \mathbf{C}_T^G\dot{\mathbf{U}}_C(t) + \mathbf{K}_T^G(t)\mathbf{U}_C(t) = \mathbf{F}_T^G(t) \tag{12}$$

The Rayleigh damping coefficients identified from an existing railway catenary [37] are adopted in the numerical model. Eq. (12) can be solved by the Newmark-β scheme. The stiffness matrix $\mathbf{K}_T^G$ is updated at each time step to adequately describe the geometrical nonlinearity and dropper slackness.

3. Aerodynamic forces

In this section, the aerodynamic forces acting on the catenary are derived based on the quasi-steady aerodynamic theory proposed by Novak [38] and Parkinson et al. [39]. In Section 3.1, the contact wire is taken as an example to illustrate the derivation procedure of aerodynamic forces. The aerodynamic coefficients used to obtain the aerodynamic force are measured by the wind tunnel test described in Section 3.2. In Section 3.3, a 3D fluctuating wind field is constructed for the catenary system.

3.1. Derivation of aerodynamic forces

Usually, the natural wind can be seen as the summation of the mean wind U and the fluctuating winds. The fluctuating wind is divided into three components: along-wind component u, crosswind component v and vertical-wind component w. Considering a

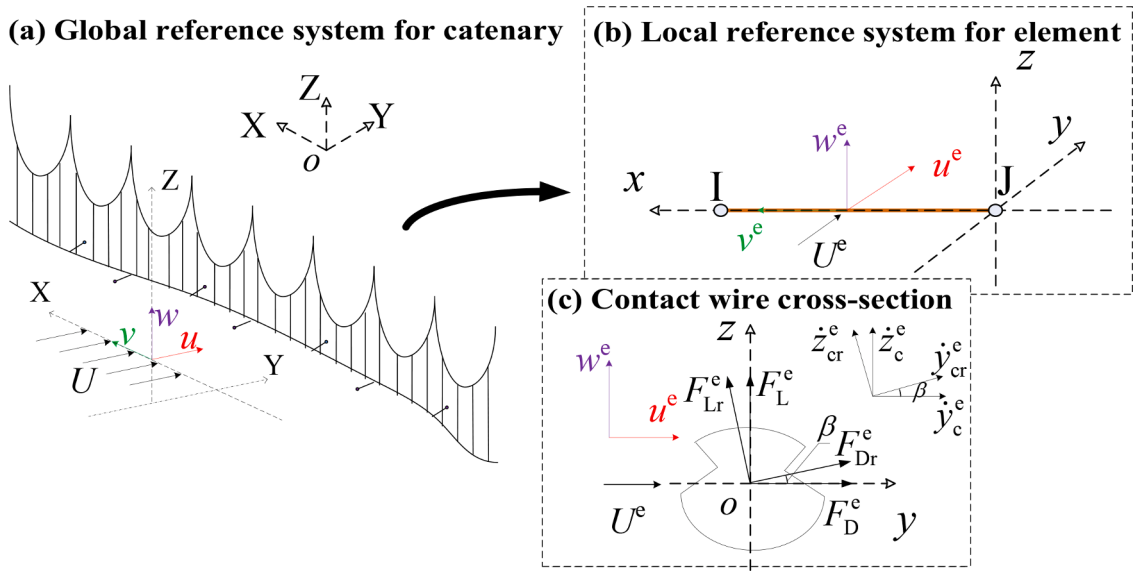

Fig. 3. Derivation of aerodynamic forces acting on contact wire: (a) Global reference system; (b) Local reference system for each element; (c) Contact wire cross section.

catenary subjected to a crosswind, as shown in Fig. 3(a), the aerodynamic forces acting on the contact wire are derived according to the following procedure. The aerodynamic forces on other components (namely, the messenger wire, dropper and steady arm) can be obtained through a similar derivation procedure.

Due to the existence of stagger values and lateral vibrations, the contact wire is not always perpendicular to the mean wind direction. The aerodynamic forces cannot be derived directly in the global reference system. As the stagger is usually several orders of magnitude smaller than the span length, a feasible solution is to transform the wind speed vectors to the local reference system for each element. The spatial transformation matrix $\mathbf{T}(\mathbf{e})$ is determined by the nodal coordinate vector $\mathbf{e}$ of each element as follows:

$$\mathbf{T}(\mathbf{e}) = \begin{bmatrix} l & m & n \\ -\dfrac{lm}{\sqrt{l^2+n^2}} & \sqrt{l^2+n^2} & -\dfrac{mn}{\sqrt{l^2+n^2}} \\ \dfrac{lm}{\sqrt{l^2+n^2}} & 0 & \dfrac{mn}{\sqrt{l^2+n^2}} \end{bmatrix} \tag{13}$$

in which

$$l = \frac{\mathbf{e}(7)-\mathbf{e}(1)}{L_e}; m = \frac{\mathbf{e}(8)-\mathbf{e}(2)}{L_e}; n = \frac{\mathbf{e}(9)-\mathbf{e}(3)}{L_e};$$
$$L_e = \sqrt{(\mathbf{e}(7)-\mathbf{e}(1))^2 + (\mathbf{e}(8)-\mathbf{e}(2))^2 + (\mathbf{e}(9)-\mathbf{e}(3))^2} \tag{14}$$

If $l = n = 0$, the transformation matrix has the following form:

$$\mathbf{T}(\mathbf{e}) = \begin{bmatrix} 0 & m & 0 \\ -m & 0 & 0 \\ 0 & 0 & 1 \end{bmatrix} \tag{15}$$

For each element, the mean wind U^e and fluctuating wind components u^e, v^e and w^e in the element local reference system can be obtained by

$$\begin{bmatrix} v^e \\ u^e \\ w^e \end{bmatrix} = \mathbf{T}(\mathbf{e}) \begin{bmatrix} v \\ u \\ w \end{bmatrix}, \begin{bmatrix} V^e \\ U^e \\ W^e \end{bmatrix} = \mathbf{T}(\mathbf{e}) \begin{bmatrix} 0 \\ U \\ 0 \end{bmatrix} \tag{16}$$

in which V^e and W^e are the longitudinal and vertical components of the mean wind in the element local reference system. According to (13) and (15), W^e always equals zero when the catenary is subjected to a crosswind U. The longitudinal components V^e and v^e can be neglected because they do not contribute to the wind-induced vibration. Considering a contact-wire cross section subjected to U^e, u^e and w^e, a sketch of the cross section is presented in Fig. 3(c). As U^e is parallel to the y-axis, "y-o-z" is called the absolute wind-axis

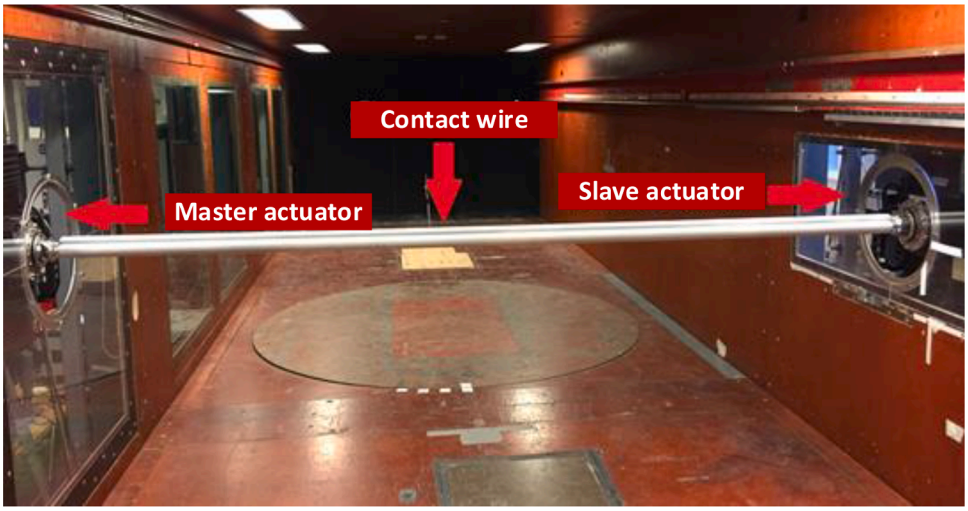

Fig. 4. Wind tunnel test for contact wire.

reference system. The drag $F_{\mathrm{D}}^{\mathrm{e}}$ and lift $F_{\mathrm{L}}^{\mathrm{e}}$ are the aerodynamic forces acting on the contact wire. According to the fluid-induced vibration theory [40], a dynamic wind angle β is induced by the movement of the contact wire subjected to the wind load, which can be estimated by

$$\beta = \arctan\left(\frac{w^{\mathrm{e}} - \dot{z}_{\mathrm{cr}}^{\mathrm{e}}}{U^{\mathrm{e}} + u^{\mathrm{e}} - \dot{y}_{\mathrm{cr}}^{\mathrm{e}}}\right) \tag{17}$$

in which $\dot{z}_{\mathrm{cr}}^{\mathrm{e}}$ and $\dot{y}_{\mathrm{cr}}^{\mathrm{e}}$ are the vertical and lateral velocities of the contact wire in the reference system (called the relative wind-axis reference system) defined by the dynamic wind angle β, lift $F_{\mathrm{Lr}}^{\mathrm{e}}$ and drag $F_{\mathrm{Dr}}^{\mathrm{e}}$. $\dot{z}_{\mathrm{cr}}^{\mathrm{e}}$ and $\dot{y}_{\mathrm{cr}}^{\mathrm{e}}$ can be obtained by transferring the vertical and lateral velocities $\dot{z}_{\mathrm{c}}^{\mathrm{e}}$ and $\dot{y}_{\mathrm{c}}^{\mathrm{e}}$ in the absolute wind-axis reference system to the relative wind-axis reference system using the following equation:

$$\begin{cases} \dot{y}_{\mathrm{cr}}^{\mathrm{e}} = \dot{y}_{\mathrm{c}}^{\mathrm{e}}\cos\beta + \dot{z}_{\mathrm{c}}^{\mathrm{e}} sin\beta \\ \dot{z}_{\mathrm{cr}}^{\mathrm{e}} = \dot{z}_{\mathrm{c}}^{\mathrm{e}}\cos\beta - \dot{y}_{\mathrm{c}}^{\mathrm{e}} sin\beta \end{cases} \tag{18}$$

$F_{\mathrm{Lr}}^{\mathrm{e}}$ and $F_{\mathrm{Dr}}^{\mathrm{e}}$ can be expressed by

$$\begin{cases} F_{\mathrm{Lr}}^{\mathrm{e}} = \dfrac{1}{2}\rho_{\mathrm{air}} U_{\mathrm{r}}^{\mathrm{e}} L_{\mathrm{e}} D C_{\mathrm{L}}(\beta) \\ F_{\mathrm{Dr}}^{\mathrm{e}} = \dfrac{1}{2}\rho_{\mathrm{air}} U_{\mathrm{r}}^{\mathrm{e}} L_{\mathrm{e}} D C_{\mathrm{D}}(\beta) \end{cases} \tag{19}$$

in which ρ_{air} is the air density. D is the diameter of the contact-wire cross section. $C_{\mathrm{L}}(\beta)$ and $C_{\mathrm{D}}(\beta)$ are the lift and drag coefficients at the angle of attack β. $U_{\mathrm{r}}^{\mathrm{e}}$ is the effective wind velocity, which can be expressed by

$$U_{\mathrm{r}}^{\mathrm{e}} = \sqrt{\left(w^{\mathrm{e}} - \dot{z}_{\mathrm{cr}}^{\mathrm{e}}\right)^2 + \left(U^{\mathrm{e}} + u^{\mathrm{e}} - \dot{y}_{\mathrm{cr}}^{\mathrm{e}}\right)^2} \tag{20}$$

According to the geometrical relationship, the drag $F_{\mathrm{D}}^{\mathrm{e}}$ and lift $F_{\mathrm{L}}^{\mathrm{e}}$ in the absolute wind-axis coordinate system can be obtained by

$$\begin{cases} F_{\mathrm{D}}^{\mathrm{e}} = F_{\mathrm{Dr}}^{\mathrm{e}}\cos(\beta) - F_{\mathrm{Lr}}^{\mathrm{e}}\sin(\beta) \\ F_{\mathrm{L}}^{\mathrm{e}} = F_{\mathrm{Dr}}^{\mathrm{e}}\sin(\beta) + F_{\mathrm{Lr}}^{\mathrm{e}}\cos(\beta) \end{cases} \tag{21}$$

The spatial coordinate transformation matrix $\mathbf{T}(\mathbf{e})$ is used again to transfer $F_{\mathrm{D}}^{\mathrm{e}}$ and $F_{\mathrm{L}}^{\mathrm{e}}$ to the global reference system, which can be directly exerted on the finite element model.

The above derivation can also be used to obtain the aerodynamic forces on the messenger wire, dropper and steady arm. It is also seen that the fluctuating components u, v, w and aerodynamic coefficients C_{D} and C_{L} should be obtained to determine the aerodynamic forces on the catenary.

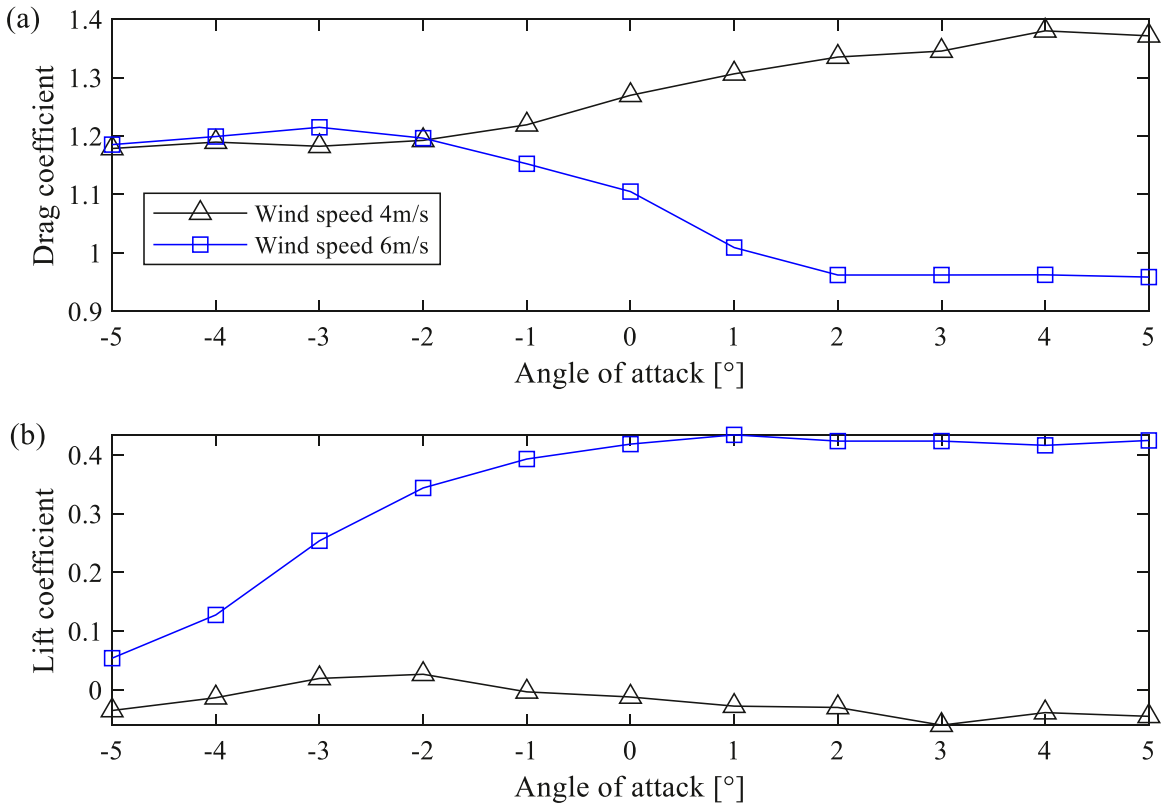

Fig. 5. Measurement results of aerodynamic coefficients for contact wire: (a) drag coefficient C_D and (b) lift coefficient C_L.

3.2. Aerodynamic coefficients

The aerodynamic coefficients are usually dependant on the cross-sectional profile and the Reynolds number. In this section, a wind tunnel test is conducted to measure the aerodynamic coefficients of a realistic contact wire subjected to a crosswind. As shown in Fig. 4, in the present experiment, the scaling ratio (between the model and prototype) of wind velocity is 1:5, while the scaling ratio of geometric size is 5:1. The Reynolds numbers ($Re = \rho UD/\mu$, where ρ is the fluid mass density, U is the wind velocity, D is the diameter of the cylinder and μ is the fluid dynamic viscosity) for the model at 4 m/s and 6 m/s are the same as the Reynolds numbers for the prototype at 20 m/s and 30 m/s, respectively. Hence, the experimentally measured C_D and C_L can be used for the full-scale prototype since these coefficients are dominated by Reynolds numbers [41]. The wind tunnel test was conducted in the Fluid Mechanics Laboratory at the Department of Energy and Process Engineering, NTNU Gløshaugen. The details of the wind tunnel test can be seen in [42].

The measurement results of C_D and C_L are presented in Fig. 5. The test wind speeds in the wind tunnel are defined as 4 m/s and 6 m/s, which correspond to 20 m/s and 30 m/s for the realistic size of a contact wire. According to the technical criteria [43], the wind deflection must be checked with a maximum wind speed of 30 m/s in the serviceability limit state. Third-order polynomials are utilised to fit the curves of the measurement parameters via the least-squares method. The explicit formulas are used in the numerical simulation to update the aerodynamic coefficients at each time step.

The cross sections for other wires (including the messenger wire, dropper and steady arm) are assumed to be circular. Therefore, the lift coefficient can be neglected. The drag coefficient C_D with different Reynolds numbers can be seen in [44].

3.3. Stochastic wind field

In this paper, the stochastic wind field is generated with the help of the open source code 'wind field simulation' [45]. The empirical spectrum is a standard method to describe the stochastics of the fluctuating wind speed. In this work, the Von Karman spectra [46] in the longitudinal, lateral and vertical directions are adopted to generate the wind speed time histories, which are presented as follows:

$$S_u(n) = \frac{4f_u\delta_u^2}{n\left(1+71f_u^2\right)^{5/6}}, f_u = \frac{nL_u}{U}$$

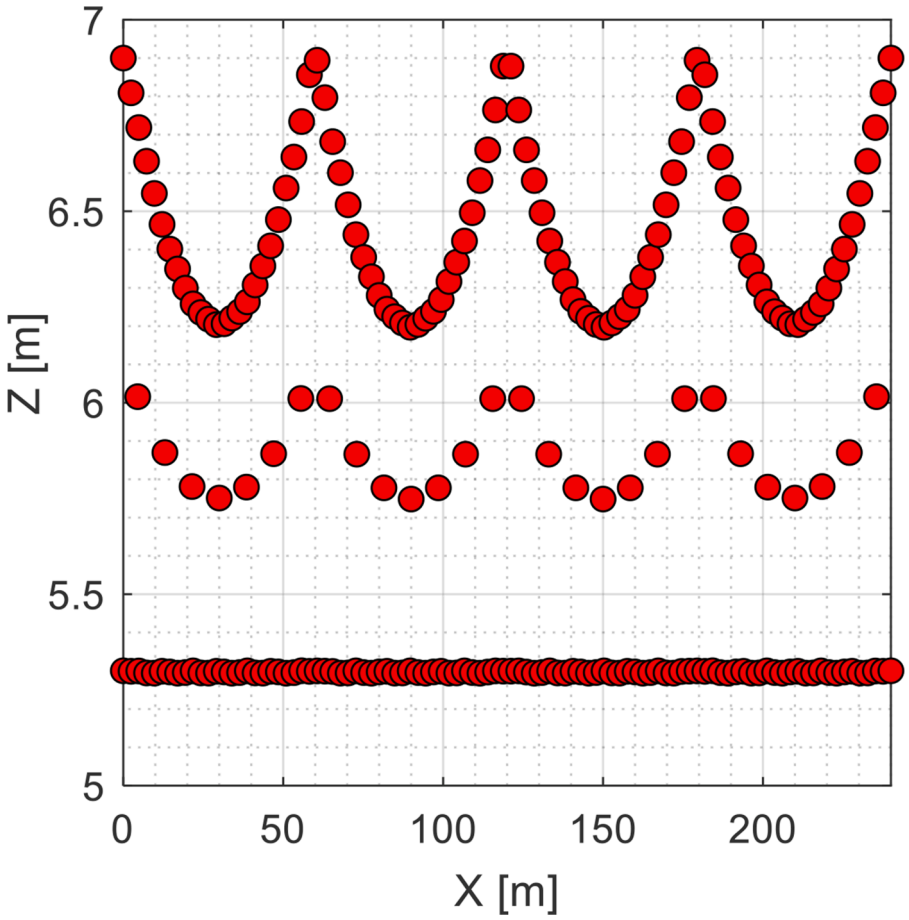

Fig. 6. Spatial grid for fluctuating wind field.

$$S_{\mathrm{v}}(n)=\frac{4f_{\mathrm{v}}\delta_{\mathrm{v}}^{2}\left(1+755f_{\mathrm{v}}^{2}\right)}{n\left(1+283f_{\mathrm{v}}^{2}\right)^{11/6}},f_{\mathrm{v}}=\frac{nL_{\mathrm{v}}}{U} \tag{22}$$

$$S_{\mathrm{w}}(n)=\frac{4f_{\mathrm{w}}\delta_{\mathrm{w}}^{2}\left(1+755f_{\mathrm{w}}^{2}\right)}{n\left(1+283f_{\mathrm{w}}^{2}\right)^{11/6}},f_{\mathrm{w}}=\frac{nL_{\mathrm{w}}}{U}$$

in which $S_{\mathrm{u}}(n)$, $S_{\mathrm{v}}(n)$ and $S_{\mathrm{w}}(n)$ are the spectra for longitudinal, lateral and vertical winds, respectively. n is the frequency. L_{u}, L_{w} and L_{v} denote the turbulence length scales in the longitudinal, lateral and vertical directions, respectively. These parameters can be chosen according to the measurement results of the crosswind along the railroad [47]. δ_{u}, δ_{w} and δ_{v} are the standard deviations of wind fluctuation in the longitudinal, lateral and vertical directions, respectively, which are determined by the turbulence intensity I_{u}, I_{w} and I_{v} by

$$\begin{cases} I_{\mathrm{u}}=\delta_{\mathrm{u}}/U \\ I_{\mathrm{v}}=\delta_{\mathrm{v}}/U \\ I_{\mathrm{w}}=\delta_{\mathrm{w}}/U \end{cases} \tag{23}$$

According to the wind-resistant design specifications [48], $I_{\mathrm{v}}=0.88I_{\mathrm{u}}$ and $I_{\mathrm{w}}=0.88I_{\mathrm{u}}$. For two arbitrary spatial points M and P, the cross-spectral density matrix for the wind components at the two points can be expressed as

$$\mathbf{S}_{\mathrm{e}}^{M,P}(\omega)=\begin{bmatrix} S_{\mathrm{uu}}^{M,P} & S_{\mathrm{uv}}^{M,P} & S_{\mathrm{uw}}^{M,P} \\ S_{\mathrm{vu}}^{M,P} & S_{\mathrm{vv}}^{M,P} & S_{\mathrm{vw}}^{M,P} \\ S_{\mathrm{wu}}^{M,P} & S_{\mathrm{wv}}^{M,P} & S_{\mathrm{ww}}^{M,P} \end{bmatrix} \tag{24}$$

in which the cross-spectral density function $S_{\varepsilon\eta}^{M,P}$ between two points M and P in the ε and η ($\varepsilon,\eta=\mathrm{u,w,v}$) directions can be expressed by

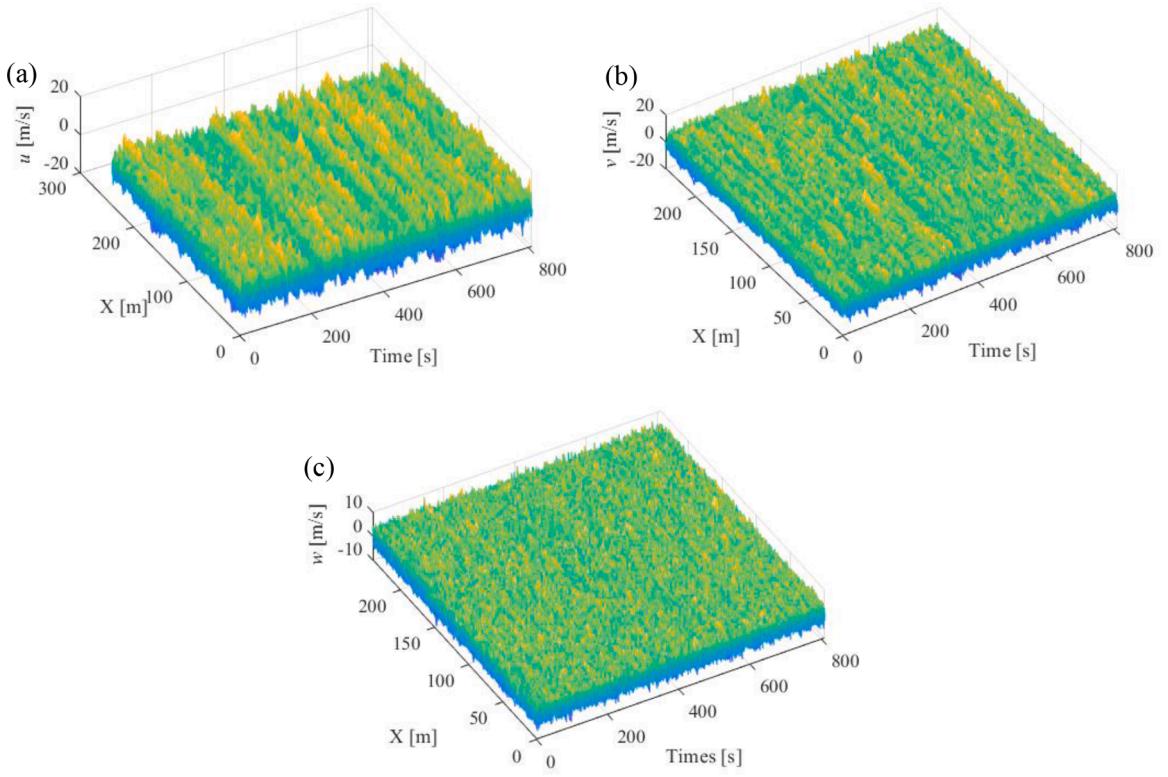

Fig. 7. Wind speed along contact wire in (a) longitudinal, (b) lateral and (c) vertical wind directions.

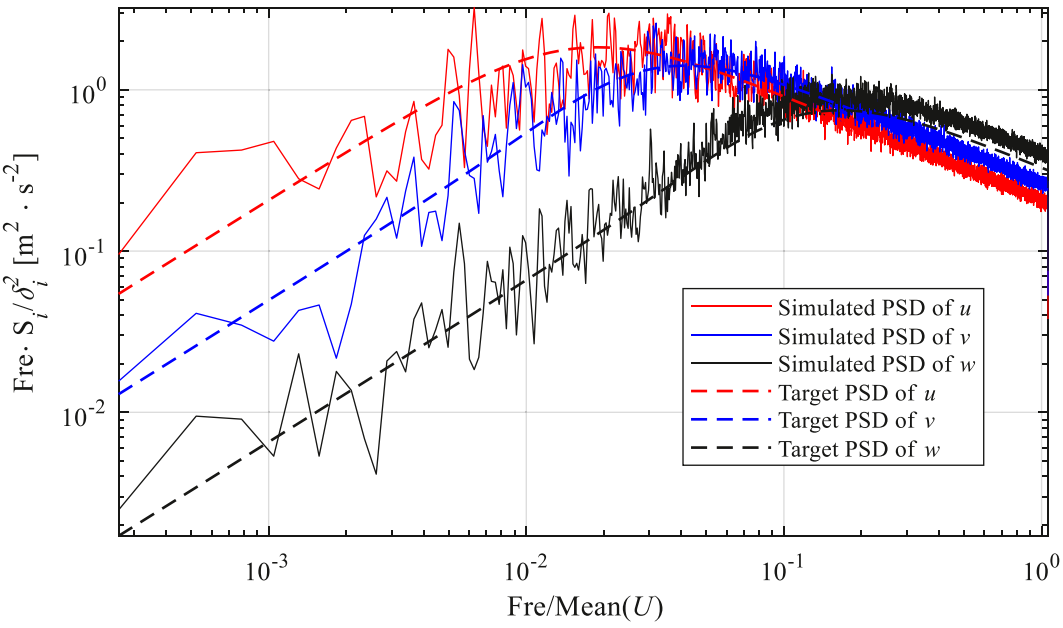

Fig. 8. Comparison between simulated and empirical spectra in (a) along-wind, (b) crosswind and (c) vertical-wind directions.

$$S_{\varepsilon\eta}^{M,P} = \sqrt{S_{\varepsilon}^{M} S_{\eta}^{P}}\,\mathrm{coh}_{\varepsilon\eta}^{M,P}, \varepsilon, \eta = \mathrm{u}, \mathrm{w}, \mathrm{v}; \tag{25}$$

where $\mathrm{coh}_{\varepsilon\eta}^{M,P}$ represents the correlation function between two points M and P in the ε and η ($\varepsilon, \eta = \mathrm{u}, \mathrm{w}, \mathrm{v}$) directions. S_{ε}^{M} denotes the spectrum at point M in the ε direction. The long-term field measurement [49] indicates that the lateral (w) component is weakly correlated to the longitudinal (u) and vertical (v) components. Therefore, it is often assumed that $\mathrm{coh}_{\mathrm{uw}}^{M,P} = 0$ and $\mathrm{coh}_{\mathrm{wv}}^{M,P} = 0$. For other cases, when $\varepsilon = \eta$,

$$\mathrm{coh}_{\varepsilon\varepsilon}^{M,P} = \exp\left(- \frac{\sqrt{C_{x\varepsilon}^2 \Delta x^2 + C_{y\varepsilon}^2 \Delta y^2 + C_{z\varepsilon}^2 \Delta z^2}}{\left(U^M + U^P\right)/2} \right) \tag{26}$$

where U^M and U^P are the mean wind velocities in the longitudinal direction at points M and P, respectively. $C_{x\varepsilon}$, $C_{y\varepsilon}$ and $C_{z\varepsilon}$ are the coherent decay coefficients for the ε component, and they are chosen from the work in [45]. When $\varepsilon \neq \eta$,

$$\mathrm{coh}_{\varepsilon\eta}^{M,P} = \sqrt{\mathrm{coh}_{\varepsilon\varepsilon}^{M,P} \mathrm{coh}_{\eta\eta}^{M,P}} \tag{27}$$

After determining an appropriate spatial grid, the global power spectral density matrix $\mathbf{S}(n)$ can be obtained by assembling Eq. (24). For the analysed catenary, the spatial grid depicted in Fig. 6 is adopted to generate the spatial wind field. The spatial grid has three layers in the vertical direction. The top one is for the messenger wire, the second is for dropper wires, and the last is for the contact wire. Then, a classical procedure employing Cholesky's decomposition and inverse Fourier transform is utilised to generate the time history of fluctuating wind speed from the spectral density matrix. Considering that the catenary is constructed on flat terrain, the turbulence intensity and the mean wind are defined as 15% and 30 m/s in the simulation [47]. One example of the wind field along the contact wire is presented in Fig. 7. The wind speed exhibits substantial variability and stochastics in each direction. The wind speed in the longitudinal direction is much higher than that in the other directions. Fig. 8 presents a comparison of the simulated and empirical spectra. The simulated spectrum exhibits good agreement with the target spectrum, verifying the acceptance of the generated wind field.

4. Maximum value estimation

Due to the stochastic nature of the buffeting response, the maximum wind deflection from a single simulation is insufficient to describe the extreme condition. It is the extreme value of the wind deflection that matters most when assessing the structural reliability due to stochastic loads. In other industrial backgrounds, e.g. bridges [50] and robotic manipulators [51], extreme value estimation is critical in safety assessments to avoid fatal accidents in extreme conditions. Therefore, the extreme value of the contact wire wind deflection should be considered in the design phase of a catenary considering its great importance for safe operation. If the response follows a Gaussian distribution, then the most widely used probability distribution $P(\eta_{\mathrm{e}})$ for extreme value η_{e} is the Poisson approximation of the extreme value distribution [52] as in the following formula. This is a classic method and has been well recognised in the industry [53,54].

$$P(\eta_{\mathrm{e}}) = \exp\left[- \nu T \exp\left(-\frac{{\eta_{\mathrm{e}}}^2}{2} \right) \right] \tag{28}$$

in which ν is the mean frequency of occurrence of zero crossings with a positive slope, which can be evaluated by

$$\nu = \frac{1}{2\pi} \left(\frac{m_2}{m_0} \right)^{1/2} \tag{29}$$

in which

$$m_\tau = \int_0^\infty f^\tau S_{\mathrm{r}}(f) \mathrm{d}f \tag{30}$$

in which $S_{\mathrm{r}}(f)$ is the power spectrum of the wind-induced vibration of the contact wire at frequency f. The mean extreme value can be derived from Eq. (28) by the approximate relation [52]

$$\overline{\eta}_{\mathrm{e}} = (2 \ln \nu T)^{1/2} + \frac{\gamma}{(2 \ln \nu T)^{1/2}} \tag{31}$$

where γ is Euler's constant, equal to 0.5772, and the standard deviation of the extreme value is given by

$$\sigma_{\eta_{\mathrm{e}}} = \frac{\pi}{\sqrt{6}} \frac{1}{(2 \ln \nu T)^{1/2}} \tag{32}$$

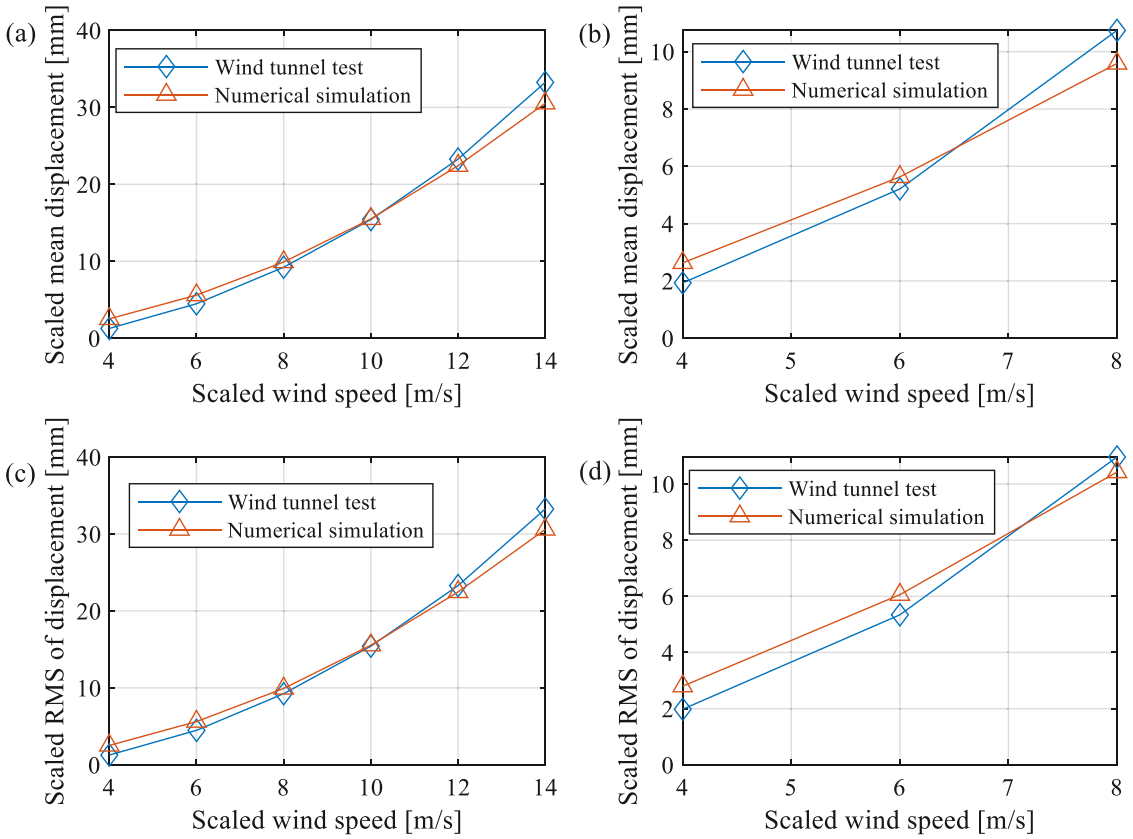

Fig. 9. Validation of numerical results against wind tunnel test: (a) scaled mean displacement with 3.1% turbulence intensity; (b) scaled mean displacement with 20% turbulence intensity; (c) scaled RMS of displacement with 3.1% turbulence intensity; (d) scaled RMS of displacement with 20% turbulence intensity.

5. Validation of numerical model

Currently, no field measurement data of the catenary's wind deflection have been reported. It is infeasible to validate the numerical model through a comparison with field data. Only Xie et al. [33] performed a wind tunnel test on an aeroelastic model of a catenary, which can be used to preliminarily validate the numerical results. In Xie et al.'s work [33], a scaled aeroelastic model of the Beijing-Shanghai high-speed railway catenary was built. The wind speed ratio was 1:2.12, and the geometry ratio was 1:4.5. Two turbulence intensities (3.1% and 20%) were used in the wind tunnel. The tests were conducted at wind speeds of 4 m/s, 6 m/s, 8 m/s, 10 m/s, 12 m/s and 14 m/s, which corresponded to realistic wind speeds of 8.48 m/s, 12.72 m/s, 16.96 m/s, 21.2 m/s, 25.44 m/s and 29.68 m/s. In this paper, a full-scale model of the same catenary is built using the method described in section 0. The wind field is simulated using the empirical spectra described in Section 3.3. Applying the aerodynamic forces derived in section 0, the wind-induced responses are simulated with the same conditions as the wind tunnel test in [33]. The simulated mean and RMS of the wind-induced response in the along-wind direction are scaled according to the geometry ratio (1:4.5). Taking the response at the midspan point as the analysis object, comparisons with the wind tunnel test results are presented in Fig. 9. Generally, the simulation results show good agreement with the wind tunnel test results. Both results show a similar trend with increasing wind speed. A larger error can be seen at a higher wind speed and higher turbulence intensity. This may be caused by the inappropriate assumption of boundary conditions and unexpected random disturbances.

6. Numerical analysis of wind-induced response

In this section, the catenary model presented in Table 1. The crosswind load derived in Section 0 is utilised to study the wind-induced response of the contact wire. The average wind speeds are chosen as 20 m/s and 30 m/s, and a typical turbulence intensity of 15% is adopted in the simulation. The central two spans are chosen as the analysis object. The total length of the simulation is 800 s, and the response of the last 600 s is analysed.

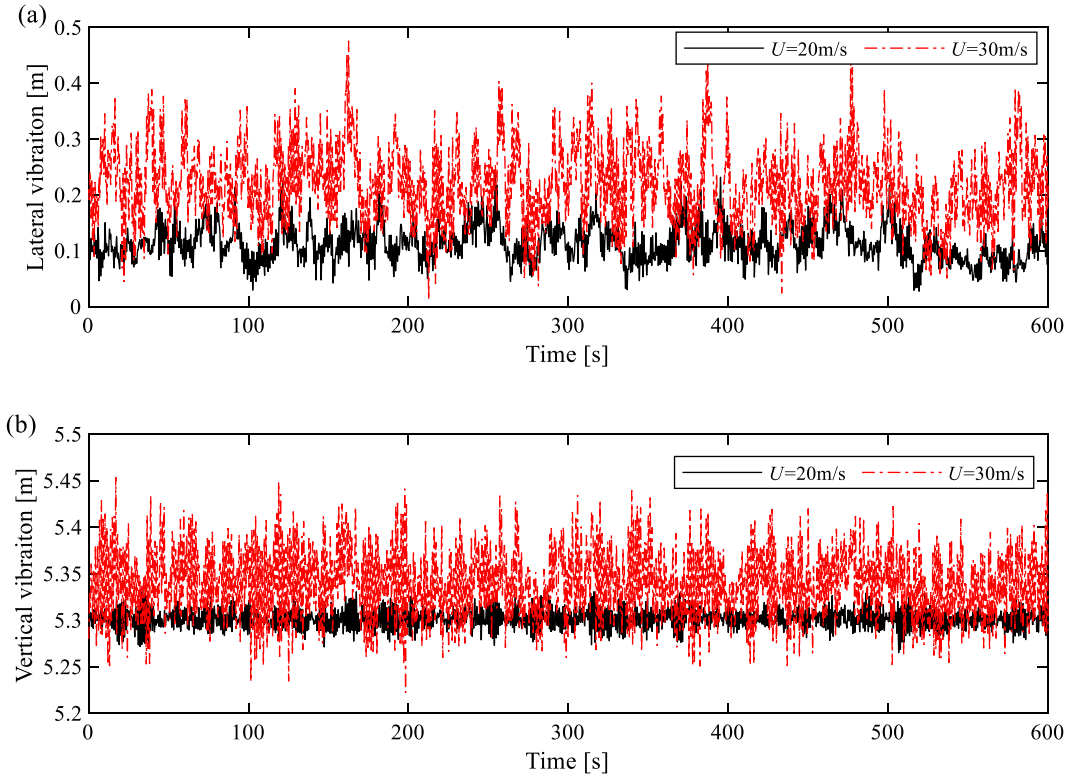

Fig. 10. Time history of midspan point displacement in (a) lateral direction and (b) vertical direction.

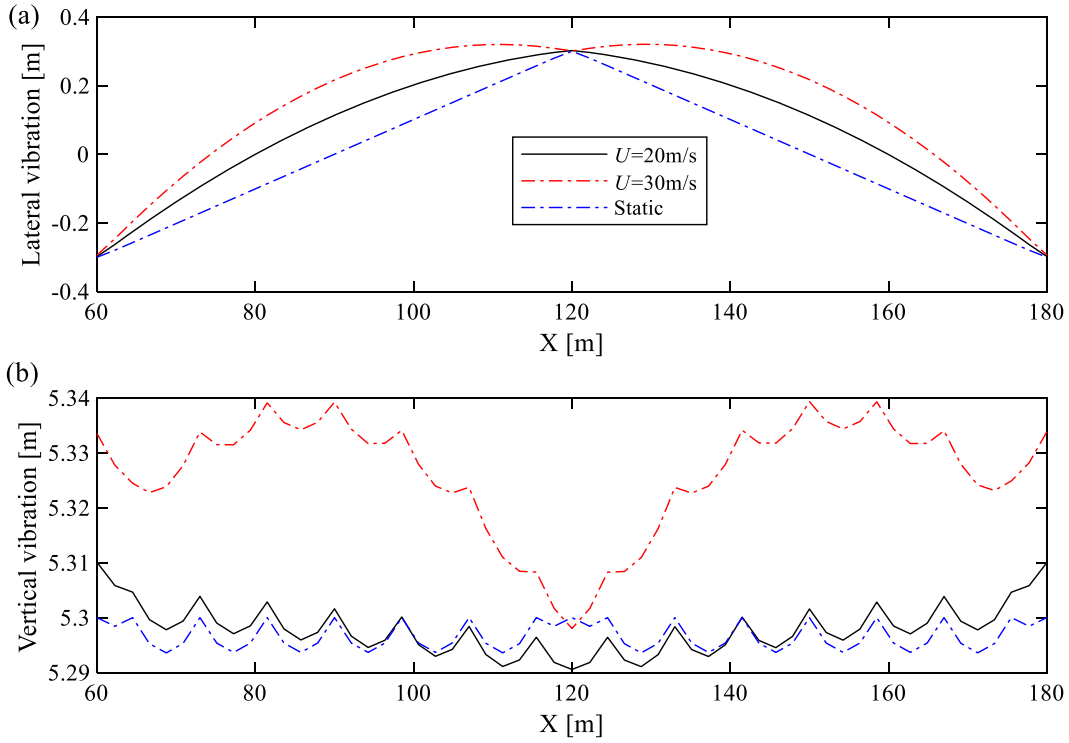

Fig. 11. Mean displacement of contact wire along two central spans in (a) lateral direction and (b) vertical direction.

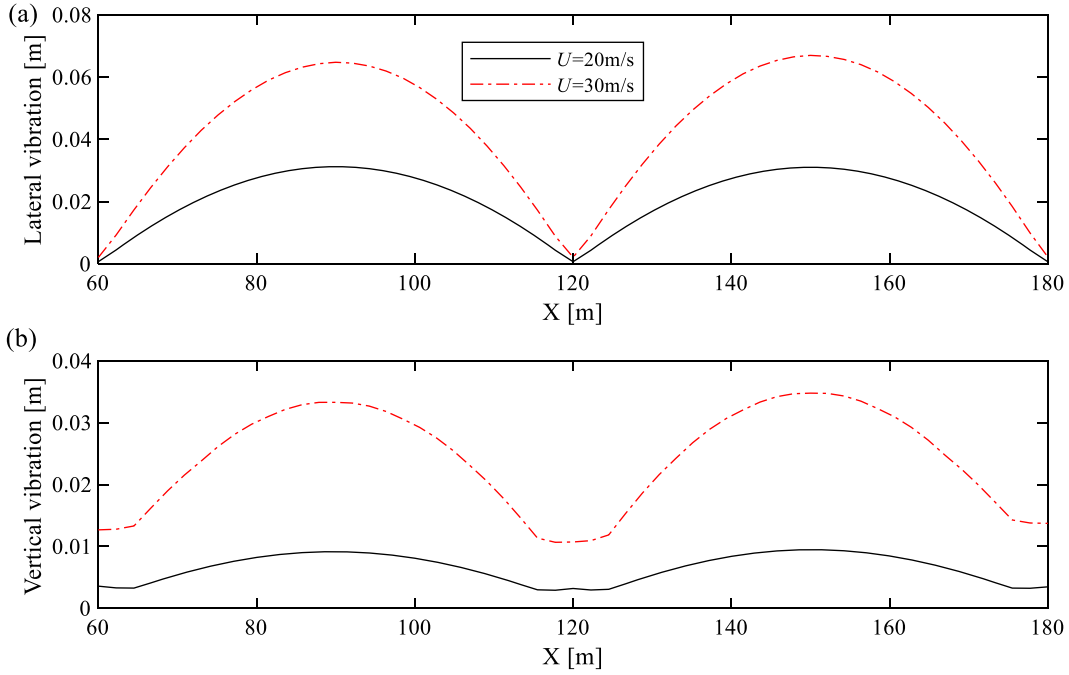

Fig. 12. Standard deviation of contact wire displacement along two central spans in (a) lateral direction and (b) vertical direction.

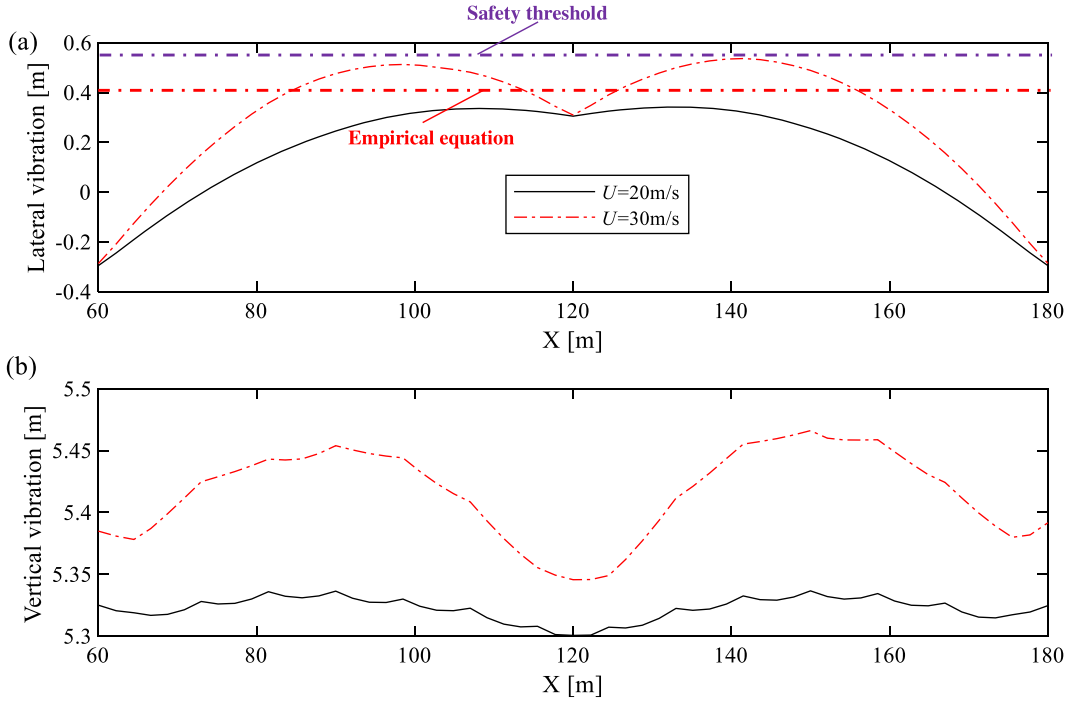

Fig. 13. Maximum value of contact wire displacement along two central spans in (a) lateral direction and (b) vertical direction.

6.1. Response analysis

The time histories of the midspan point displacement in the lateral and vertical directions are presented in Fig. 10(a) and (b), respectively. Considering that the initial position of the contact wire in the midspan point is zero, the crosswind leads to a significant lateral deviation. The mean lateral displacement reaches 0.113 m and 0.216 m with mean wind speeds of 20 m/s and 30 m/s,

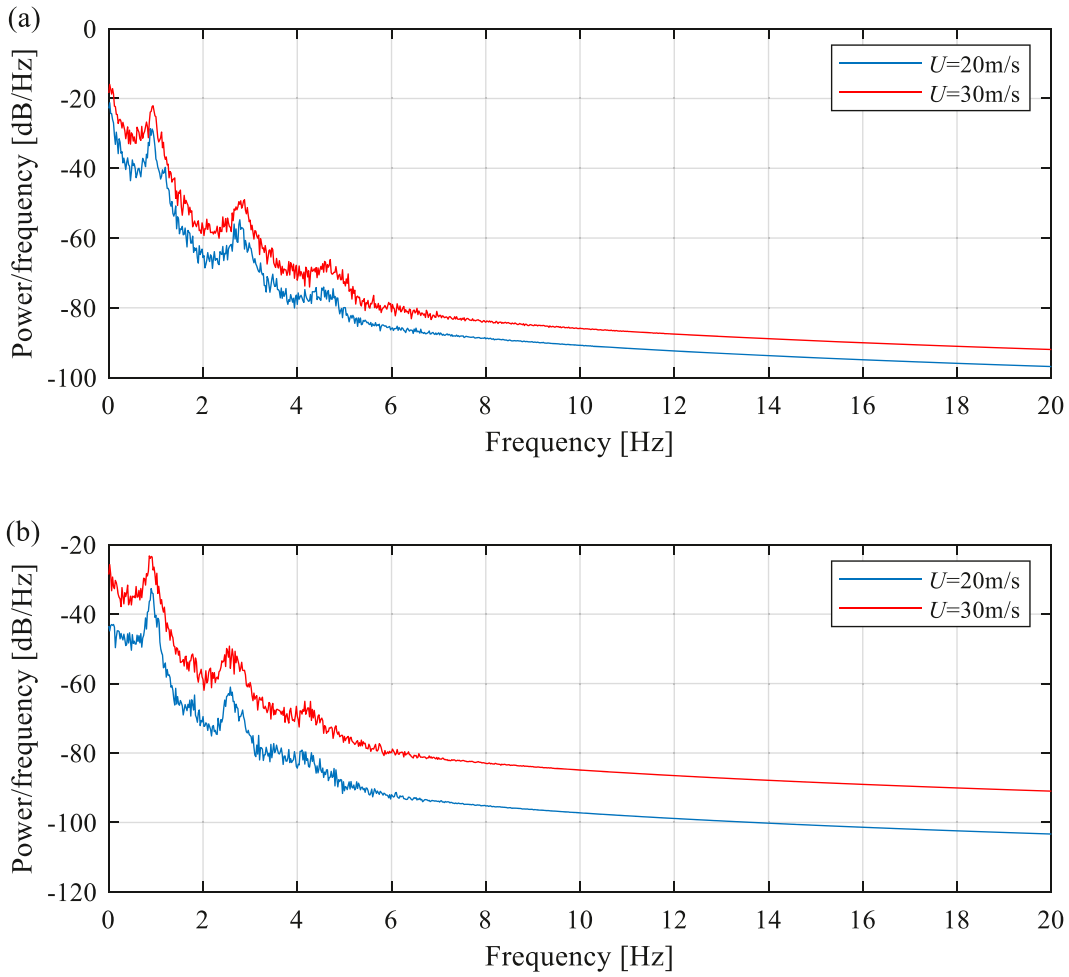

Fig. 14. Spectra of contact wire displacement in (a) lateral direction and (b) vertical direction.

respectively. The corresponding maximum displacement reaches 0.245 m and 0.475 m with mean wind speeds of 20 m/s and 30 m/s, respectively. In the vertical direction, the wind deflection is much smaller than in the lateral direction. The maximum deviation reaches only 0.15 m against the initial position.

6.2. *Statistical analysis*

Some critical statistical indices (including the mean, standard deviation and maximum value) of the contact wire displacement are analysed in this section. Fig. 11 shows the mean displacement of the contact wire along two central spans in the lateral and vertical directions. The mean wind U mainly causes the mean wind deflection. The maximum mean deflection does not exceed the stagger value (0.3 m) in the lateral direction when $U = 20$ m/s. When $U = 30$ m/s, the maximum mean deflection reaches 0.32 m at the positions of 111 m and 131 m. The mean deflection is much smaller in the vertical direction than in the lateral direction because the lift coefficient is significantly smaller than the drag coefficient, as shown in Fig. 5. Mainly when $U = 20$ m/s, the mean deflection is almost the same as the initial configuration.

The contribution of the fluctuating wind can be estimated by the standard deviation of the contact wire vibration. Fig. 12 presents the standard deviation of the contact wire displacement along two central spans. Unlike the mean deflection, the maximum standard deviation appears in the midspan for both the lateral and vertical vibrations. The minimum standard deviation occurs around the steady arm due to the constraint in the lateral direction. Fig. 13 presents the maximum value of the contact wire displacement. In the vertical direction, the maximum wind deflection appears at the midspan, and the minimum wind deflection occurs around the steady arm. The distribution of the maximum vertical deflection is not as smooth as that in the lateral direction due to the uneven distribution of the stiffness caused by droppers. Due to the existence of the stagger value in the lateral direction, the maximum displacement does not appear at the midspan. When $U = 20$ m/s, the maximum displacement occurs at approximately 9 m from the steady arm (located at 120 m). When U increases to 30 m/s, the maximum displacement moves closer to the midspan point, which appears at approximately 21.5 m from the steady arm. According to the technical specification [43], the wind deflection safety of the contact wire should be

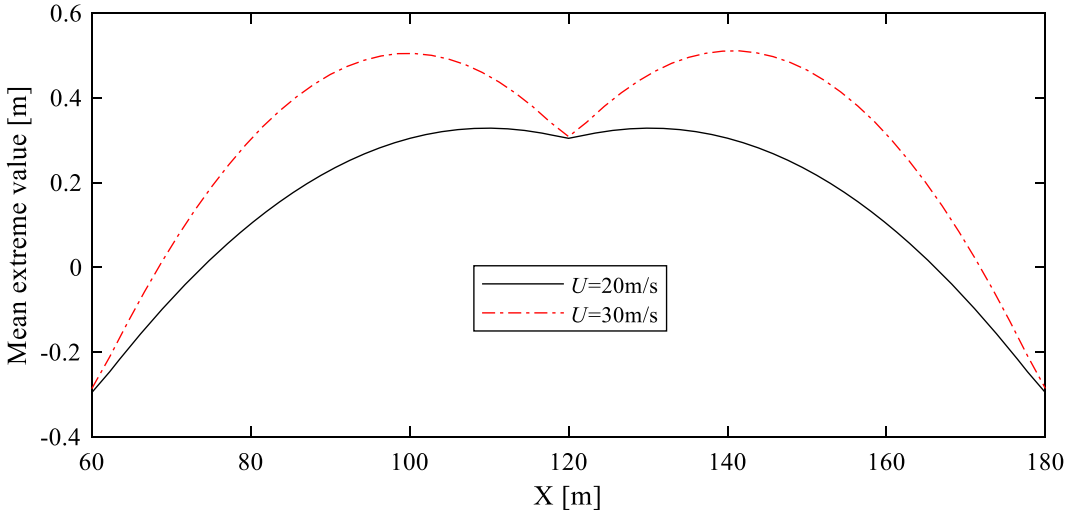

Fig. 15. Mean extreme value of lateral contact wire displacement.

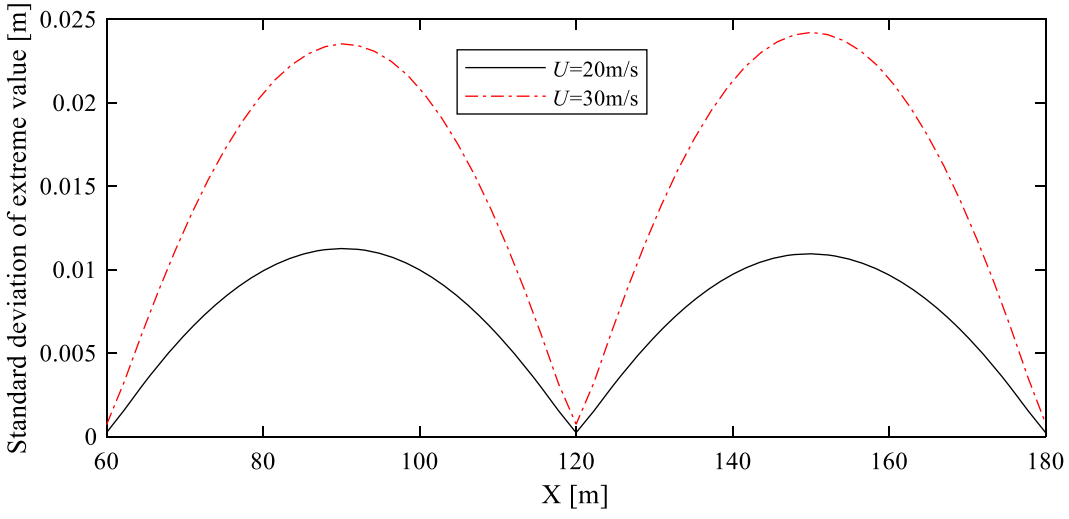

Fig. 16. Standard deviation of extreme value of lateral contact wire displacement.

evaluated at a wind speed of 30 m/s. The maximum wind deflection in the lateral direction reaches 0.513 m at 98.5 m and 141.5 m, which is smaller than the maximum permissible lateral deviation of 0.55 m specified in En 50,367 [55]. However, note that the maximum wind deflection estimated by Eq. (2) is only 0.405 m, which is smaller than the present FEM result and may result in dangerous consequences. The shortcoming of the empirical equation is that fluctuating wind is not sufficiently taken into account when estimating the wind deflection.

6.3. *Frequency analysis*

Fig. 14(a) and (b) present the contact wire displacement spectra in the lateral and vertical directions, respectively. The spectrum has three significant peaks at approximately 0.9 Hz, 2.8 Hz and 4.7 Hz, which correspond to the first three groups of the natural frequency of the catenary. This finding is consistent with the work in [56], which indicates that the buffeting behaviour of the catenary is dominated by the first three groups of intrinsic modes. The resulting spectrum can be substituted into Eq. (30) to estimate the extreme value of the wind deflection in Section 0.

6.4. *Extreme value estimation*

Using the standard deviation and spectrum obtained in the above sections, the mean and standard deviation of the extreme value can be estimated using Eqs. (31) and (32). Only the lateral extreme value is estimated in this section, as it has the potential to cause

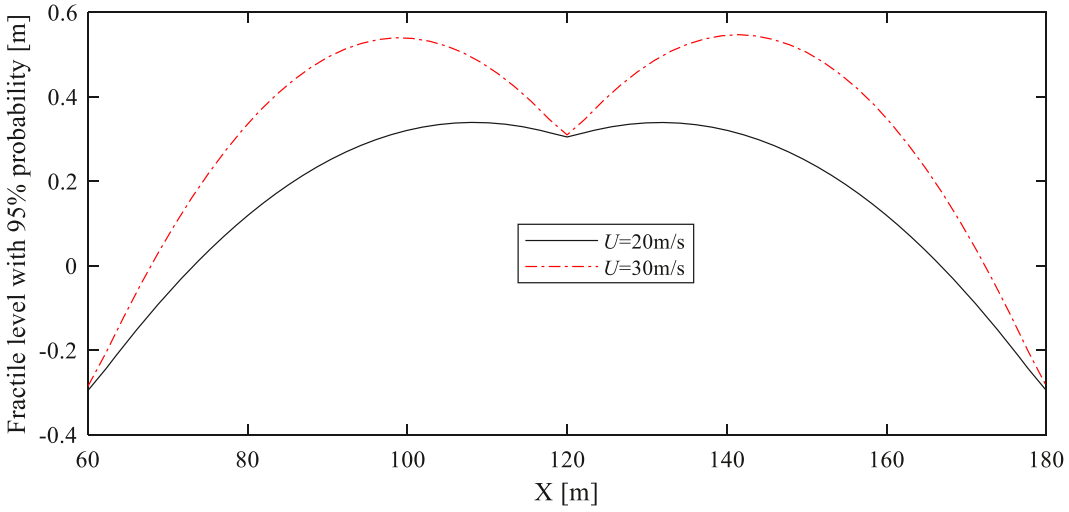

Fig. 17. Fractile level with 95% probability of extreme value of lateral contact wire displacement.

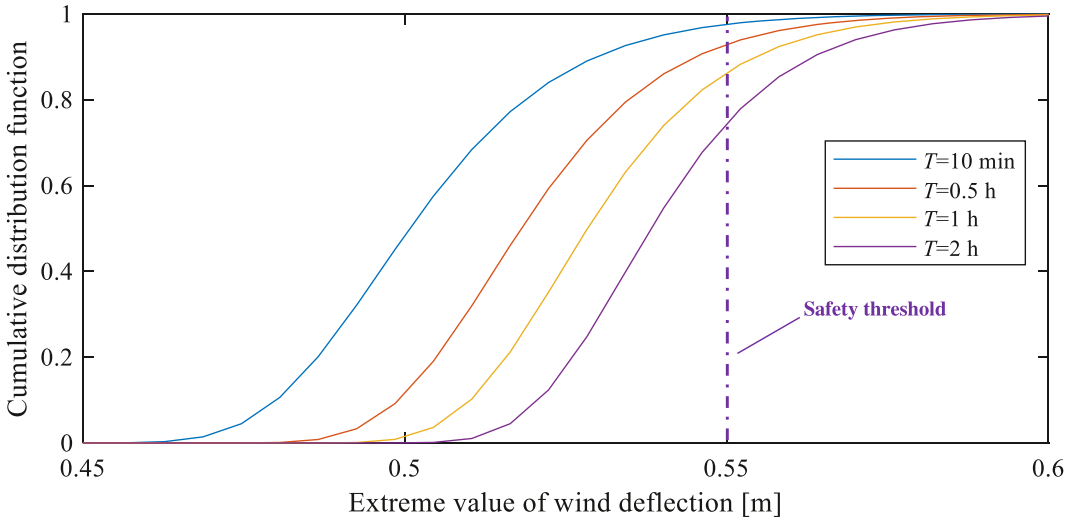

Fig. 18. Cumulative distribution function of extreme values of lateral contact wire displacement at different durations of fluctuating wind.

fatal accidents. Considering a 10-minute gust wind, the mean extreme value of the lateral contact wire displacement along the central two spans is presented in Fig. 15. The maximum mean extreme value appears at the same positions as the maximum mean displacement shown in Fig. 11(a). The maximum mean extreme value with $U = 30$ m/s reaches 0.505 m at positions of approximately 111 m and 131 m. The corresponding standard deviation of the extreme value is presented in Fig. 16. The extreme value of lateral displacement has a large fluctuation at the midspan. The maximum standard deviation can reach 0.0235 m when $U = 30$ m/s. Using the probability distribution function in Eq. (28), the fractile level with a 95% probability of extreme value (which can represent the maximum extreme value with a 95% confidence level [57]) is presented in Fig. 17. The largest wind deflection appears at 98.5 m and 141.5 m, which are consistent with the actual maximum wind deflection shown in Fig. 13(a). However, due to the stochastic nature of the fluctuating wind, the maximum wind deflection can reach 0.54 m with a 95% confidence level, which is 5.26% higher than the actual maximum wind deflection of 0.513 in Fig. 13(a).

To perform a probabilistic analysis of the extreme value of wind deflection, the cumulative distribution functions of the extreme value with different fluctuating wind durations are presented in Fig. 18. Considering a safety threshold of 0.55 m [55], 97.8% of the extreme values are lower than the safety limit when the catenary is subjected to a 10-minute fluctuating wind. However, this percentage drops to 92.5%, 84.2% and 73.1% when the fluctuating wind duration increases to 0.5 h, 1 hour and 2 h, respectively. Therefore, a long-duration gust of wind can significantly increase the possibility of the contact wire's wind deflection, thus exceeding

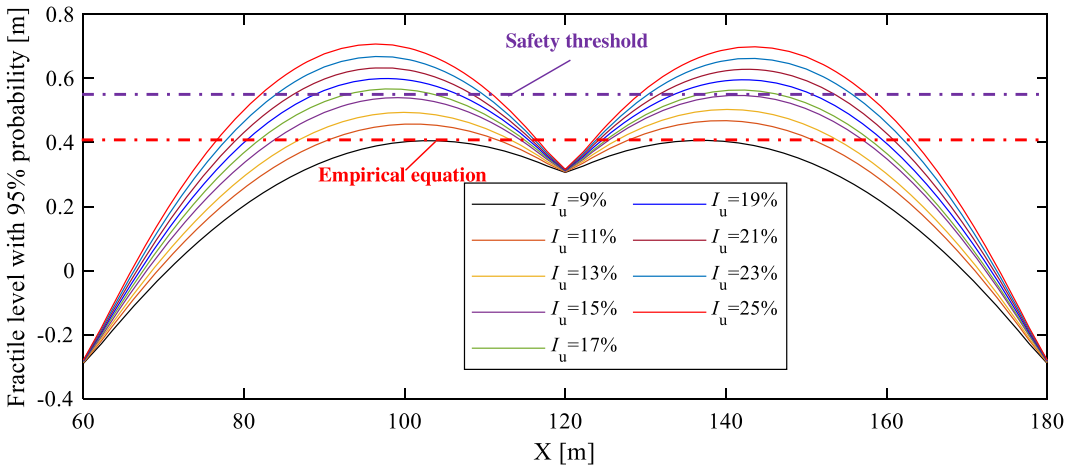

Fig. 19. Fractile level with 95% probability of extreme value of lateral contact wire displacement at different turbulence intensities.

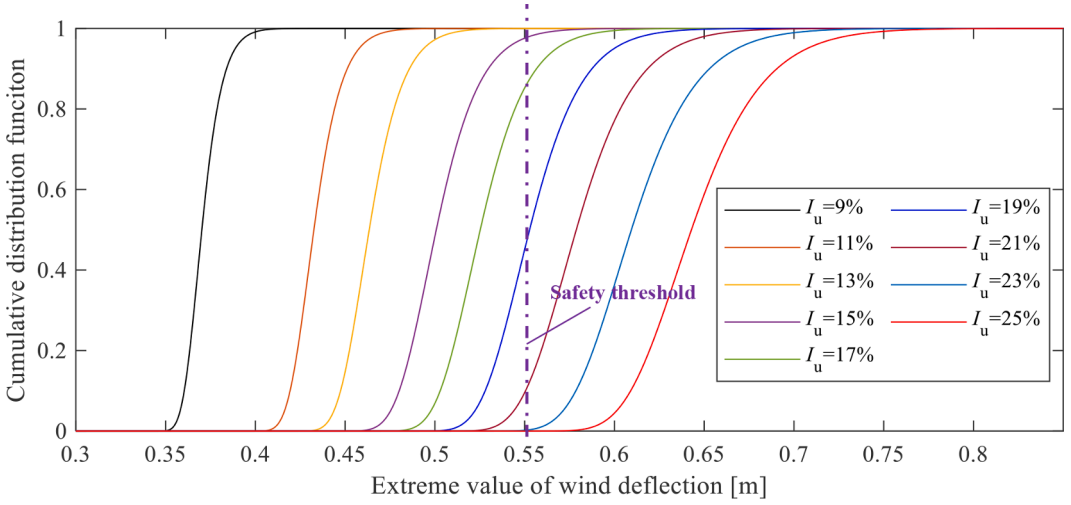

Fig. 20. Cumulative distribution function of extreme value at position where maximum wind deflection occurs at different turbulence intensities.

the safety limit. Currently, the safety of the contact wire's wind deflection is only assessed with a gust wind duration of no more than 10 min [34]. The risk caused by the long-duration gust wind deserves special attention when designing railways that cross specific wind zones.

7. Effects of turbulence intensity

The turbulence intensity is mainly determined by the terrain categories. For open terrain, the turbulence intensity is usually lower than 20%. However, for some complex terrains such as mountainous area, a significant turbulence intensity may appear. According to the field measurement result [58], the turbulence intensity can reach over 20% for some complex terrains. In this section, the contact wire's wind deflection safety is assessed with different I_u ranging from 9% to 25% with a 2% interval. The mean wind speed U is chosen as 30 m/s in the simulation according to the design specification [34].

Fig. 19 presents the fractile level with a 95% probability of extreme value (which represents the maximum extreme value at a 95% confidence) with different turbulence intensities. When the turbulence intensity is no more than 15%, the maximum extreme value of the lateral contact wire displacement cannot exceed the safety threshold of 0.55 m at a 95% confidence level. At turbulence intensities of 17%, 19%, 21%, 23% and 25%, the maximum extreme values can reach 0.57 m, 0.60 m, 0.63 m, 0.67 m and 0.71 m, respectively, which exceed the safety threshold and may result in dewirement accidents. The maximum wind deflection estimated by Eq. (2) is almost the same as the FEM result at a 9% turbulence intensity. When the turbulence intensity is higher than 9%, the empirical equation may underestimate the wind deflection and lead to risky results. Note that the position of the maximum wind deflection varies with the change in turbulence intensity. The lower the turbulence intensity, the closer the position of the maximum wind deflection to the steady arm. By contrast, the maximum wind deflection is closer to the midspan at a higher turbulence intensity. The

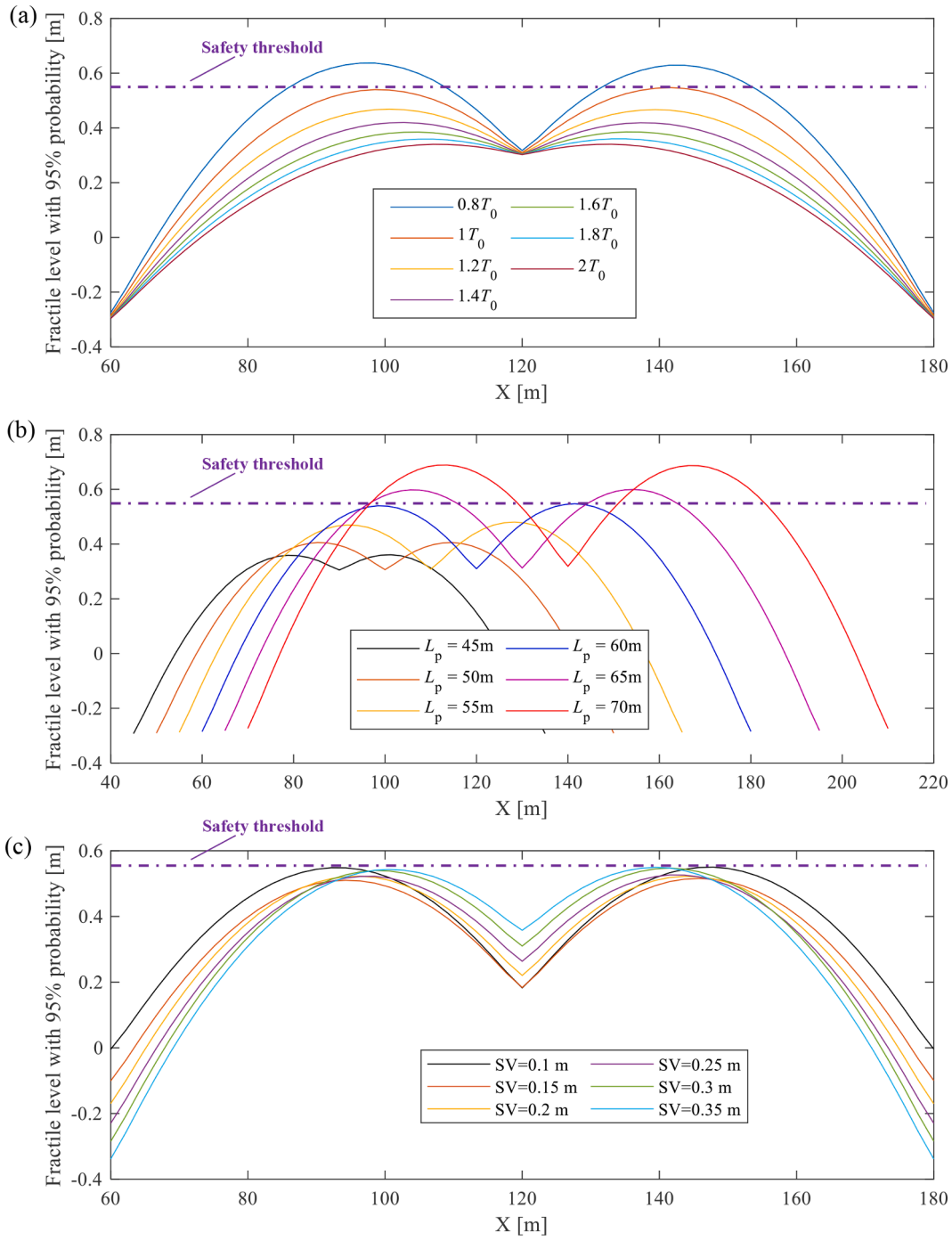

Fig. 21. Fractile level with 95% probability of extreme value of lateral contact wire displacement with different (a) tension classes; (b) span lengths; (c) stagger values.

cumulative distribution function of the extreme value at the position where maximum wind deflection occurs for each case is presented in Fig. 20. Through a comparison with the safety threshold, it is seen that almost 100% of extreme values are within the safety limit at a turbulence intensity smaller than 15%. However, this percentage drops to 85% and 45% at turbulence intensities of 17% and 19%, respectively. When the turbulence intensity is higher than 20%, the most extreme values are no longer within the safety limit for the analysed catenary. More attention should be given when designing the catenary in complex terrains to avoid fatal accidents caused by unsteady wind with a significant turbulence intensity.

8. Effects of structural parameters

In this section, the effects of key structural parameters (including the tension, span length and stagger value) of the catenary on the contact wire's wind deflection are analysed. The even wind speed is chosen as 30 m/s as above. The turbulence intensity is defined as 15%, representing the most common case. The fractile level with a 95% probability of the extreme value of the lateral contact wire displacement is adopted as the primary assessment index for each parameter to represent the potential maximum extreme value. Tension is the most important parameter for a catenary, as it directly determines the maximum operating speed of the train. Seven tension classes are adopted in the numerical simulation: 0.8, 1, 1.2, 1.4, 1.6, 1.8 and 2 times the original tension T0. Fig. 21(a) shows the fractile level with a 95% probability of the extreme value of the lateral contact wire displacement with different tension classes. It can be clearly observed that an increase in the tension class can effectively reduce the wind deflection of the contact wire. The maximum wind deflections are smaller than the safety threshold except for the deflection with 0.8 times the original tension. This occurs because the dewirement and scraping of pantograph collectors mostly occur in old railways, which potentially causes tension loss in the catenary. It is also seen that the position of the maximum wind deflection varies with a change in tension. The higher the tension, the closer the position of the maximum wind deflection to the steady arm.

According to the design specification [43], the span length of a catenary typically ranges from 45 m to 70 m. This specification is adopted in the simulation. The results are presented in Fig. 21(b). The contact wire's wind deflection undergoes a significant increase with increasing span length. The maximum wind deflections exceed the safety threshold when the span length is over 65 m.

At the ends of each span, the contact wire is mounted at a fixed lateral displacement with respect to the track centreline. This is called a stagger value. The stagger value changes from 0.1 m to 0.35 m in the simulation, and the results are presented in Fig. 21(c). The change in stagger value does not primarily affect the maximum wind deflection occurring around the midspan point. Generally, an increase in the stagger value causes a slight rise in wind deflection. However, the catenary with a minimal stagger value (0.1 m) has the largest maximum wind deflection. When a minimal stagger value is set, the steady arm has more space to rotate, which releases the constraint in the lateral direction and results in a large wind deflection. When the stagger value is greater than 0.15 m, an increase in the stagger value leads to a monotonous increase in the maximum wind deflection. For the sake of wind deflection safety, a relatively small stagger value is preferred. However, the stagger value cannot be too small to restrict the lateral displacement of the support point.

9. Conclusions

This paper presented an assessment of the catenary's wind deflection based on wind tunnel experiments and nonlinear finite element models. The aerodynamic forces acting on the catenary were derived according to quasi-steady aerodynamic theory. The aerodynamic coefficients were obtained through a wind tunnel test. The extreme value of the contact wire's wind deflection was estimated based on an empirical probability distribution. The main conclusions are drawn as follows:

1) The maximum wind deflection estimated by the empirical equation was generally the same as the FEM result when the turbulence intensity was 9%. However, when the turbulence intensity 9%, the empirical equation could produce a risky result.
2) A long-duration gust wind can significantly reduce the reliability of the catenary system. Currently, the safety of the contact wire's wind deflection was only assessed with a gust wind duration of no longer than 10 min. The risk caused by the long-duration gust wind deserves special attention when designing railways crossing specific wind zones.
3) When the turbulence intensity is greater than 20%, most extreme values of the wind deflection are no longer within the safety limit for the analysed catenary. More attention should be given when designing the catenary in complex terrains to avoid fatal accidents caused by unsteady wind with a significant turbulence intensity.
4) An increase in tension and decrease in span length can effectively reduce the maximum wind deflection. A reduction in the stagger value can slightly reduce the maximum wind deflection. However, the stagger value cannot be too small to restrict the lateral displacement of the support point.

Note that the change in structural parameters may also influence the interaction performance of the pantograph-catenary. Generally, an increase in tension has a positive effect on contact quality. However, the effect of span length on the interaction performance is complex and deserves further investigation. Note also that the numerical model is only partially validated due to the missing alignment between the wind tunnel test and simulation assumptions. Field data should be collected in the future to fully validate the numerical model.

Declaration of Competing Interest

The authors declare no conflict of interest.

Acknowledgment

The work presented in this paper was funded by the Norwegian Railway Directorate.

References

[1] S. Bruni, G. Bucca, M. Carnevale, et al., Pantograph–catenary interaction: recent achievements and future research challenges, Int. J. Rail Transp. 6 (2018) 57–82.
[2] M. Zhang, F. Xu, Y. Han, Assessment of wind-induced nonlinear post-critical performance of bridge decks, J. Wind Eng. Ind. Aerodyn. (2020) 203.
[3] R.H. Scanlan, The action of flexible bridges under wind, II: buffeting theory, J. Sound Vib. 60 (1978) 201–211.
[4] C. Chen, C. Mannini, G. Bartoli, et al., Experimental study and mathematical modeling on the unsteady galloping of a bridge deck with open cross section, J. Wind Eng. Ind. Aerodyn. 203 (2020), 104170.
[5] M. Zhang, F. Xu, O. Øiseth, Aerodynamic damping models for vortex-induced vibration of a rectangular 4:1 cylinder: comparison of modeling schemes, J. Wind Eng. Ind. Aerodyn. (2020) 205.
[6] R.H. Scanlan, The action of flexible bridges under wind, I: flutter theory, J. Sound Vib. 60 (1978) 187–199.
[7] Y.M. Desai, P. Yu, N. Popplewell, et al., Finite element modelling of transmission line galloping, Comput. Struct. 57 (1995) 407–420.
[8] Y. Song, Z. Liu, H. Wang, et al., Analysis of the galloping behaviour of an electrified railway overhead contact line using the non-linear finite element method, Proc. Inst. Mech. Eng. Part F J. Rail Rapid Transit 232 (2018) 2339–2352.
[9] Z. Lu, X. Wang, K. Yue, et al., Coupling model and vibration simulations of railway vehicles and running gear bearings with multitype defects, Mech. Mach. Theory 157 (2021), 104215.
[10] P. Urda, J.F. Aceituno, S. Muñoz, et al., Artificial neural networks applied to the measurement of lateral wheel-rail contact force: a comparison with a harmonic cancellation method, Mech. Mach. Theory 153 (2020), 103968.
[11] Z. Wang, G. Mei, Q. Xiong, et al., Motor car–track spatial coupled dynamics model of a high-speed train with traction transmission systems, Mech. Mach. Theory 137 (2019) 386–403.
[12] H. Chen, B. Jiang, S.X. Ding, et al., Data-driven fault diagnosis for traction systems in high-speed trains: a survey, challenges, and perspectives, IEEE Trans. Intell. Transp. Syst. (2020) 1–17.
[13] W. Liu, Z. Liu, Y. Li, et al., An automatic loose defect detection method for catenary bracing wire components using deep convolutional neural networks and image processing, IEEE Trans. Instrum. Meas. (2021) 70.
[14] F. Marques, H. Magalhães, J. Pombo, et al., A three-dimensional approach for contact detection between realistic wheel and rail surfaces for improved railway dynamic analysis, Mech. Mach. Theory 149 (2020), 103825.
[15] H. Kim, Z. Hu, D. Thompson, Effect of cavity flow control on high-speed train pantograph and roof aerodynamic noise, Railw. Eng. Sci. 28 (2020) 54–74.
[16] W. Zhang, D. Zou, M. Tan, et al., Review of pantograph and catenary interaction, Front. Mech. Eng. 13 (2018) 311–322.
[17] O.V. Van, J.P. Massat, C. Laurent, et al., Introduction of variability into pantograph-catenary dynamic simulations, Veh. Syst. Dyn. 52 (2014) 1254–1269.
[18] P. Zdziebko, A. Martowicz, T. Uhl, An investigation on the active control strategy for a high-speed pantograph using co-simulations, Proc. Inst. Mech. Eng. Part I J. Syst. Control Eng. 233 (2019) 370–383.
[19] Y. Song, Z. Wang, Z. Liu, et al., A spatial coupling model to study dynamic performance of pantograph-catenary with vehicle-track excitation, Mech. Syst. Signal Process 151 (2021), 107336.
[20] J. Gil, S. Gregori, M. Tur, et al., Analytical model of the pantograph–catenary dynamic interaction and comparison with numerical simulations, Veh. Syst. Dyn. (2020) 1–24.
[21] Y. Song, A. Rønnquist, T. Jiang, et al., Identification of short-wavelength contact wire irregularities in electrified railway pantograph–catenary system, Mech. Mach. Theory 162 (2021), 104338.
[22] F. Vesali, M.A. Rezvani, H. Molatefi, et al., Static form-finding of normal and defective catenaries based on the analytical exact solution of the tensile Euler–Bernoulli beam, Proc. Inst. Mech. Eng. Part F J. Rail Rapid Transit 233 (2019) 691–700.
[23] Y. Song, P. Antunes, J. Pombo, et al., A methodology to study high-speed pantograph-catenary interaction with realistic contact wire irregularities, Mech. Mach. Theory 152 (2020), 103940.
[24] Y. Song, Z. Liu, A. Ronnquist, et al., Contact wire irregularity stochastics and effect on high-speed railway pantograph-catenary interactions, IEEE Trans. Instrum. Meas. 69 (2020) 8196–8206.
[25] Z. Xu, Y. Song, Z. Liu, Effective measures to improve current collection quality for double pantographs and catenary based on wave propagation analysis, IEEE Trans. Veh. Technol. 69 (2020) 6299–6309.
[26] Y. Song, Z. Liu, Z. Xu, et al., Developed moving mesh method for high-speed railway pantograph-catenary interaction based on nonlinear finite element procedure, Int. J. Rail Transp. 7 (2019) 173–190.
[27] S. Kulkarni, C.M. Pappalardo, A.A. Shabana, Pantograph/Catenary contact formulations, J. Vib. Acoust. Trans. ASME 139 (2017), 011010.
[28] Y. Song, A. Rønnquist, P. Nåvik, Assessment of the high-frequency response in railway pantograph-catenary interaction based on numerical simulation, IEEE Trans. Veh. Technol. 69 (2020) 10596–10605.
[29] J. Pombo, J. Ambrosio, M. Pereira, et al., Influence of the aerodynamic forces on the pantograph-catenary system for high-speed trains, Veh. Syst. Dyn. 47 (2009) 1327–1347.
[30] J. Pombo, J. Ambrosio, Environmental and track perturbations on multiple pantograph interaction with catenaries in high-speed trains, Comput. Struct. 124 (2013) 88–101.
[31] Y. Song, Z. Liu, H. Wang, et al., Nonlinear analysis of wind-induced vibration of high-speed railway catenary and its influence on pantograph–catenary interaction, Veh. Syst. Dyn. 54 (2016) 723–747.
[32] Y. Song, Z. Liu, F. Duan, et al., Study on wind-induced vibration behavior of railway catenary in spatial stochastic wind field based on nonlinear finite element procedure, J. Vib. Acoust. Trans. ASME 140 (2018), 011010–1–14.
[33] Q. Xie, X. Zhi, Wind tunnel test of an aeroelastic model of a catenary system for a high-speed railway in China, J. Wind Eng. Ind. Aerodyn. 184 (2019) 23–33.
[34] J. Wu, Pantograph and contact line system, editor, in: G Jones (Ed.), Pantogr. Contact Line Syst, Chengdu: Southwest Jiaotong University Publisher, 2017.
[35] European Committee for Electrotechnical Standardization. EN 50119. Railway applications — Fixed installations — Electric traction Overhead Contact Lines, European Standards (EN), Brussels, 2015.
[36] H.K. Kim, M.Y. Kim, Efficient combination of a TCUD method and an initial force method for determining initial shapes of cable-supported bridges, Int. J. Steel Struct. 12 (2012) 157–174.
[37] P. Nåvik, A. Rønnquist, S. Stichel, Identification of system damping in railway catenary wire systems from full-scale measurements, Eng. Struct. 113 (2016) 71–78.
[38] M. Novak, Galloping oscillations of prismatic structures, ASCE J. Eng. Mech. Div. 98 (1972) 27–46.
[39] G.V. Parkinson, J.D. Smith, The square prism as an aeroelastic non-linear oscillator, Q. J. Mech. Appl. Math. 17 (1964) 225–239.
[40] T.J. Scanion, M.T. Stickland, A.B. Oldroyd, An investigation into the attenuation of wind speed by the use of windbreaks in the vicinity of overhead wires, Proc. Inst. Mech. Eng. Part F J. Rail Rapid Transit 214 (2000) 173–182.
[41] C. Norberg, Fluctuating lift on a circular cylinder: review and new measurements, J. Fluids Struct. 17 (2003) 57–96.
[42] A.R. Elvebakken, Estimation of Aerodynamic Forces On a Railway Contact Wire and Their Effect On Galloping Instability-Wind Tunnel Testing of an AC-120 Contact Wire, NTNU, 2018.
[43] F. Kiessling, R. Puschmann, A. Schmieder, et al., Contact Lines For Electric Railways, 3rd edition, John Wiley & Sons, 2018. Third Edit. eb - Elektrische Bahnen.

[44] H. Schlichting, K. Gersten, Boundary-layer Theory, Springer, Berlin Heidelberg, 2016.
[45] Cheynet E. Wind field simulation (text-based input) [Internet]. 2020. Available from: https://github.com/ECheynet/windSim_textBased.
[46] E.E. Morfiadakis, G.L. Glinou, M.J. Koulouvari, The suitability of the von Karman spectrum for the structure of turbulence in a complex terrain wind farm, J. Wind Eng. Ind. Aerodyn. 62 (1996) 237–257.
[47] Y.L. Xu, Q.S. Ding, Interaction of railway vehicles with track in cross-winds, J. Fluids Struct. 22 (2006) 295–314.
[48] JTG/T3360-01-2018, Wind-resistant Design Specification For Highway Bridges (in Chinese), China Commun. Press, Beijing, China, 2018.
[49] G. Solari, G. Piccardo, Probabilistic 3-D turbulence modeling for gust buffeting of structures, Probabilistic Eng. Mech. 16 (2001) 73–86.
[50] Y. Gu, S. Li, H. Li, et al., A novel Bayesian extreme value distribution model of vehicle loads incorporating de-correlated tail fitting: theory and application to the Nanjing 3rd Yangtze River Bridge, Eng. Struct. 59 (2014) 386–392.
[51] Q. Zhao, J. Guo, J. Hong, et al., An enhanced moment-based approach to time-dependent positional reliability analysis for robotic manipulators, Mech. Mach. Theory 156 (2021), 104167.
[52] A.G. Davenport, Note on the distribution of the largest value of a random function with application to gust loading, Proc. Inst. Civ. Eng. (1964).
[53] S. Coles, J. Heffernan, J. Tawn, Dependence measures for extreme value analyses, Extrem 2 (1999) 339–365.
[54] S.Y. Novak, On the accuracy of Poisson approximation, Extremes (Boston) 22 (2019) 729–748.
[55] European Committee for Electrotechnical Standardization, EN 50367. Railway applications — Current collection Systems — Technical criteria For the Interaction Between Pantograph and Overhead Line, European Standards (EN), Brussels, 2016.
[56] Y. Song, M. Zhang, H. Wang, A response spectrum analysis of wind deflection in railway overhead contact lines using pseudo-excitation method, IEEE Trans. Veh. Technol. 70 (2021) 1169–1178.
[57] G. Michaelov, S. Sarkani, L.D. Lutes, Fractile levels for non-stationary extreme response of linear structures, Struct. Saf. 18 (1996) 11–31.
[58] C.A. Martins, O.L.L. Moraes, O.C. Acevedo, et al., Turbulence intensity parameters over a very complex terrain, Boundary-Layer Meteorol. 133 (2009) 35–45.